

GCA-TR-67-11-N

MEASUREMENT OF UPPER ATMOSPHERIC IONIZATION
AND WINDS WITH A COMBINED PAYLOAD

L.G. Smith
J.F. Bedinger
G.T. Best
E. Constantinides

GCA CORPORATION
GCA TECHNOLOGY DIVISION
Bedford, Massachusetts

FINAL REPORT

Contract No. NASw-1083

June 1967

Prepared for
NATIONAL AERONAUTICS AND SPACE ADMINISTRATION
Headquarters
Washington, D.C.

TABLE OF CONTENTS

<u>Title</u>	<u>Page</u>
INTRODUCTION	1
ROCKET FLIGHTS	5
WIND AND ELECTRON DENSITY PROFILES AT FORT CHURCHILL	9
AIRCRAFT OBSERVATIONS AT FORT CHURCHILL	19
UPPER ATMOSPHERE TEMPERATURES DEDUCED FROM OBSERVATIONS OF AN A ₂ O TRAIL AT TWILIGHT	37
OBSERVATIONS DURING THE SOLAR ECLIPSE OF 12 NOVEMBER 1966	49
CONCLUSIONS AND RECOMMENDATIONS	59
REFERENCES	65
APPENDIX A - TIME-DEPENDENT REDISTRIBUTION THEORY	69
APPENDIX B - VEHICLE PERFORMANCE DATA	77

INTRODUCTION

The principal scientific objective of this contract is the study of the relation between the structure of the electron density profile and of the wind in the E region. In particular it is an investigation of the wind shear theory of sporadic E proposed by Whitehead [1]* and developed by MacLeod [2] and others. The theory, in its simplest form, postulates that a layer of enhanced electron density will form at the point of zero velocity of an east-west wind shear of the appropriate sign (one in which the wind is toward the east on the lower side of the layer and toward the west on the upper side of the layer). This theory has been formally presented only as a steady-state solution of the distribution equation and thus can compare only the relative positions of observed layers and wind profiles. (A preliminary version of a time-dependent theory is given in Appendix A).

Comparison of detailed profiles from vapor trails and rocket probes shows that some layers are associated with wind shear as required by the theory, but that others are not. Also, it is found that the observed ionized layers do not have the cusp-like shape predicted by the theory. In addition, laboratory values of recombination coefficients for the principal ions of the E region (i.e. NO^+ and O_2^+) are an order of magnitude larger than those required by the theory. The initial formulation of the theory has been expanded to include polarization fields and metallic ions in an attempt to give better agreement with observations. As yet however, there is no convincing interpretation of the phenomenon.

Good agreement with the wind-shear theory is reported by MacLeod [2], and Wright et al [3] who compared sporadic-E heights obtained from ground-based ionosondes with the ion drift computed from the neutral winds observed from vapor trails.

Poor agreement with theory is reported by Bedinger and Knafllich [4] who find that 14 out of 17 layers of enhanced ionization observed with rocket probes showed a random relation to wind shears but coincided with corners on corresponding wind hodographs. The association of layers with corners on the wind profile suggests a relation between the location of the layers and the second derivative of the horizontal wind with respect to altitude. The importance of these discontinuities has recently been discussed by Layzer [5] but subsequently refuted by Whitehead [6].

The present series of observations was aimed at examining the wind shear theory of the formation of sporadic E layers at high latitudes, specifically at Fort Churchill in the auroral zone, and in Brazil during the total solar eclipse of 12 November 1966.

Other objectives of the program included measurement of upper atmosphere temperatures using the fluorescence spectrum of aluminum oxide, and observations of the comet Ikeya-Seki [7] using a one-half meter Fastie spectrometer.

*Numbers in [] denote reference.

A further phase of the program was a determination of the feasibility of using an aircraft to replace the ground stations for observation of the winds and determination of temperature.

In another phase of the contract two payloads were delivered to the Indian Government for launch from the Thumba Rocket Range. The first of these was successfully launched during March 1967 and performed perfectly. At the request of the Indian INCOSPAR scientists the second payload was intentionally not flown at that time in order to allow detailed study of its construction by their engineers. Some components were removed from this second payload by the Indians for use in their own payloads.

A summary of technical reports, journal articles and presentations at scientific meeting of the results of this program is given in Table 1.

TABLE 1

REPORTS AND ARTICLES ON CONTRACT NO. NASw-1083

Journal Articles and Conference Proceedings

- Bedinger, J.F. and H.B. Knafllich, "Observed Characteristics of Ionospheric Winds," Radio Science 1, pp. 156-168 (1966).
- Smith, L.G., "Rocket Observations of Sporadic E and Related Features of the E Region," Radio Science 1, pp. 178-186 (1966).
- Smith, L.G., "Summary and Conclusions from the Estes Park Sporadic E - Rocket Measurements," Radio Science 1, pp. 244-245 (1966).
- Bedinger, J.F. and L.G. Smith, "Measured Wind Shears and Electron Densities," Space Research VII, North-Holland Publishing Co., Amsterdam (1967).
- Coté, O.R., "Turbulence and Eddy Coefficients Deduced from Vapor Trails," Space Research VII, North-Holland Publishing Co., Amsterdam (1967).

GCA Technical Reports

- Corman, A. and N.J. Guarino, "Canister for Producing TMA Trails in the Upper Atmosphere," GCA Technical Report No. 65-2-N (February 1965).
- Coté, O.R., "Turbulent Diffusion of Sodium Vapor Trails in the Upper Atmosphere," GCA Technical Report No. 65-5-N (March 1965).
- Smith, L.G., "Rocket Observations of Sporadic E and Related Features of the E Region," GCA Technical Report No. 65-22-N (August 1965).
- Bedinger, J.F. and H.B. Knafllich, "Observed Characteristics of Ionospheric Winds," GCA Technical Report No. 65-26-N (August 1965).
- Bedinger, J.F., "Compendium of Wind Data from the Vapor Trail Technique," GCA Technical Report No. 66-7-N (March 1966).
- Smith, L.G., J.F. Bedinger, and G.T. Best, "Measurement of Upper Atmospheric Ionization and Winds with a Combined Payload," GCA Technical Report No. 66-11-N (June 1966).
- Best, G.T., "Upper Atmosphere Temperature Determination Using A₂O Bands Excited by the Sun at Twilight," GCA Technical Report No. 67-7-N (May 1961).
-

TABLE 1 (continued)

Presentations at Scientific Meetings

Bedinger, J. F. and H. B. Knafllich, "Small Scale Structure Observed in Vapor Trails Around 100 km," paper presented at the Second Conference on Direct Aeronomic Measurements in the Lower Ionosphere, University of Illinois, 27-30 (September 1965).

Smith, L. G., "Rocket Observation of Sporadic E and Related Features of the E Region," paper presented at the URSI Fall Meeting, Dartmouth College, 4-6 (October 1965).

Bedinger, J. F. and L. G. Smith, "Measured Wind Shears and Electron Densities," presented at the COSPAR Symposium on Interaction Between the Neutral Part and the Ionized Part of the Atmosphere, on 17 May 1966 in Vienna.

Coté, O. R., "Turbulence and Eddy Coefficients Deduced from Vapor Trails," presented at the COSPAR Symposium on Interaction Between the Neutral Part and the Ionized Part of the Atmosphere, on 18 May 1966 in Vienna.

ROCKET FLIGHTS

Nineteen payloads were constructed during this program. At the time this report is being prepared all but two have been launched. Two payloads remain: one as noted in the previous section is in possession of Indian scientists and engineers; the second, not necessary to the objectives of the final series of observations on the contract, is being held for future use.

The payloads are in two parts: a lower section containing the canister and timing circuits and an upper section containing the probe, an aspect magnetometer, and telemetry system. The two sections of the payload are electrically independent for reasons of safety and reliability. The vapor release is initiated near apogee and continues during descent of the rocket.

Table 2 contains a summary of the seventeen flights conducted under this program. All used Nike Apaches rockets. The date, time, and place of launch is given. This is followed by the type of vapor used for the wind measurement: either Trimethylaluminum (TMA) or a mixture of sodium and lithium (Na-Li). The apogee altitude is indicated where it is known. Note that Nike Apache 14.282 carried a payload consisting only of a TMA vapor section; no probe section could be included because of scheduling problems.

Vehicle performance data on the launches through the series of October 1965 has been given in a previous report [7]. Available data on the subsequent flights is given in Appendix B, which also reports the work with radar transponder beacons on Nike Apaches 14.278 through 14.281.

A brief account of the field trip to Ft. Churchill in September 1966 follows. Twilight trails of both sodium and TMA were planned in order that temperature might be determined from each. A group of French scientists observed both trails with equipment designed to measure temperature. The TMA trail was observed by GCA personnel with a spectrophotometer loaned by W.G. Fastie, of John Hopkins University.

Another major phase of the operation concerned the feasibility of using an aircraft as an observational platform instead of ground sites. The NASA Electra (NASA-927) from Houston was at Ft. Churchill from 11 to 16 September 1966 and gave excellent support during all firings.

Ground camera sites were established at Belcher, Seal River, Twin Lakes, Caribou River, and at the NRC auroral site.

The weather forecast for 13 September 1966 was favorable and a combined probe and sodium vapor payload was fired during evening twilight on Nike-Apache 14.278. All instrumentation performed satisfactorily and good data were obtained from the plane as well as the ground stations. The weather remained clear and the second rocket (14.279) of the series carrying a probe-TMA payload was launched one hour and forty eight minutes later at 2223 CST. The probe section of this payload performed well but no TMA trail was observed.

TABLE 2

SUMMARY OF ROCKET LAUNCHES CONTRACT NASw-1083

Nike Apache	Date	Time	Launch	Vapor	Apogee
14.195	7 Oct. '64	1804 EST	W.I.*	TMA	172 km
14.194	8 Oct. '64	0523 EST	W.I.	Na-Li	160 km
14.197	1 Nov. '64	0000 CST	F.C.**	Na-Li	165 km
14.196	27 Feb. '65	1821 CST	F.C.	Na-Li	155 km
14.198	27 Feb. '65	2130 CST	F.C.	TMA	Vehicle Failed
14.199	28 Feb. '65	0000 CST	F.C.	TMA	Vehicle Failed
14.200	28 Feb. '65	0611 CST	F.C.	TMA	Vehicle Failed
14.201	22 June '65	2300 EST	W.I.	TMA	167 km
14.202	5 Oct. '65	1821 CST	F.C.	TMA	181 km
14.203	5 Oct. '65	2100 CST	F.C.	TMA	Vehicle Failed
14.278	13 Sep. '66	1935:22 CST	F.C.	Na-Li	156 km
14.279	13 Sep. '66	2223 CST	F.C.	TMA†	181 km
14.280	15 Sep. '66	1922 CST	F.C.	TMA	185 km
14.281	15 Sep. '66	2100 CST	F.C.	TMA	185 km
14.282‡	15 Sep. '66	2217 CST	F.C.	TMA	Not Yet Known
14.77	12 Nov. '66	1402 UT	Brazil	TMA	185 km
10.12	12 Mar. '67	2230 LST	India	TMA	Not Yet Known

* W.I. - Wallops Island, Va.

** F.C. - Fort Churchill, Man.

† No vapor release occurred.

‡ No probe section was carried on this flight.

Subsequent analysis of the telemetry record revealed that the disturbance of the probe signal which always occurs during ejection was not present. The cause of failure of TMA ejection is not known. This is the only failure of the system in over twenty flights.

Clouds obscured ground sites before the next scheduled firing and the series was terminated.

A brief period of clear skies was again present during the early evening of 15 September. Largely due to weather reconnaissance by the NASA aircraft, it was possible to utilize the temporary clearing condition for completion of the firings: The series began at twilight, 1922 CST with Nike Apache 14.280 carrying a combined probe-TMA payload. All phases of the experiment were successful. Results of winds, electron density, electron temperature, and neutral temperature are given in subsequent sections of the report. The results of observations by French scientists are not known.

The third launching in this series was Nike-Apache 14.282 fired at 2217 CST which did not have a probe but ejected a trail of TMA and good wind measurements were obtained.

The field trip to Brazil for the launch of Nike Apache 14.77 during the total solar eclipse is described in a later section of this report.

The field trip to India for the launch of Nike Apache 10.12 was accomplished without incident.

WIND AND ELECTRON DENSITY PROFILES AT FORT CHURCHILL

Hodographs of the winds obtained from the four vapor trails are shown in Figures 1 through 4. The winds on 13 September 1966, Figure 1, are typical of the profiles often observed at many launch sites. The outstanding feature is the large spiral pattern with small scale features such as corners and shears. The series of profiles on 15 September have the spiral structure at lower altitudes, but show the development of a reversal in wind direction in the upper region. A reversal in the direction of rotation with height is found on hodographs from many sites. The spiral pattern at the lower heights remains intact throughout the observing interval and the nearly closed loop appears to be rotating clockwise with time. The small scale differences in the patterns prevent a meaningful point-to-point comparison on the successive profiles, but the open segment of the loop appears to be directed to about 330 deg. in the earliest profile and to about 50 deg. in the last profile. This is a rotation of 80 deg. in three hours which is equivalent to the expected rotation imposed by the Coriolis parameter at 60 deg. latitude.

The hodograph from 2100 CST, 15 September, Figure 3, has an unusual number of regions of high shear. The highest shear, nearly 100 m/sec-km, is only rarely observed but occurs at 99 km both in Figure 1 and Figure 3 and at nearly the same location on the hodograph.

Electron density profiles obtained during the same two nights are shown in Figures 5 through 8. The quantity plotted is probe current, measured at 2.7 volt. Comparison with electron density values obtained on previous occasions from ionosonde and propagation experiments shows that above about 100 km the current is proportional to electron density and a mean value of $1.2 \times 10^{10} \text{ cm}^{-3} \text{ amp}^{-1}$ can be obtained for the ratio of electron density to current. The absolute values of electron density shown are accurate to about ± 20 percent although the relative accuracy for each profile separately is no more than 5 percent (i.e. this is the accuracy of the actual current measurement). Below 100 km, the ratio of electron density to current decreases and at 80 km is less than that at 100 km by a factor of about 3.

A profile is obtained up to the time that vapor release is initiated, which usually takes place near apogee. In one flight (14.279) the vapor release did not occur and a profile was obtained during rocket descent. The difference between ascent and descent profiles above 95 km on this flight is largely attributable to a wake effect and is seen in all launches at high elevation angles (i.e. about 85 degrees). The difference between ascent and descent profiles is thus believed to be a local effect at the probe and should not be interpreted as caused by horizontal gradients of electron density. Similarly the peak in current at about 95 km on the descent profile is probably not a real layer in electron density.

The two profiles taken on the night of 13-14 September 1966, separated by nearly three hours, are in close agreement in the magnitude of electron

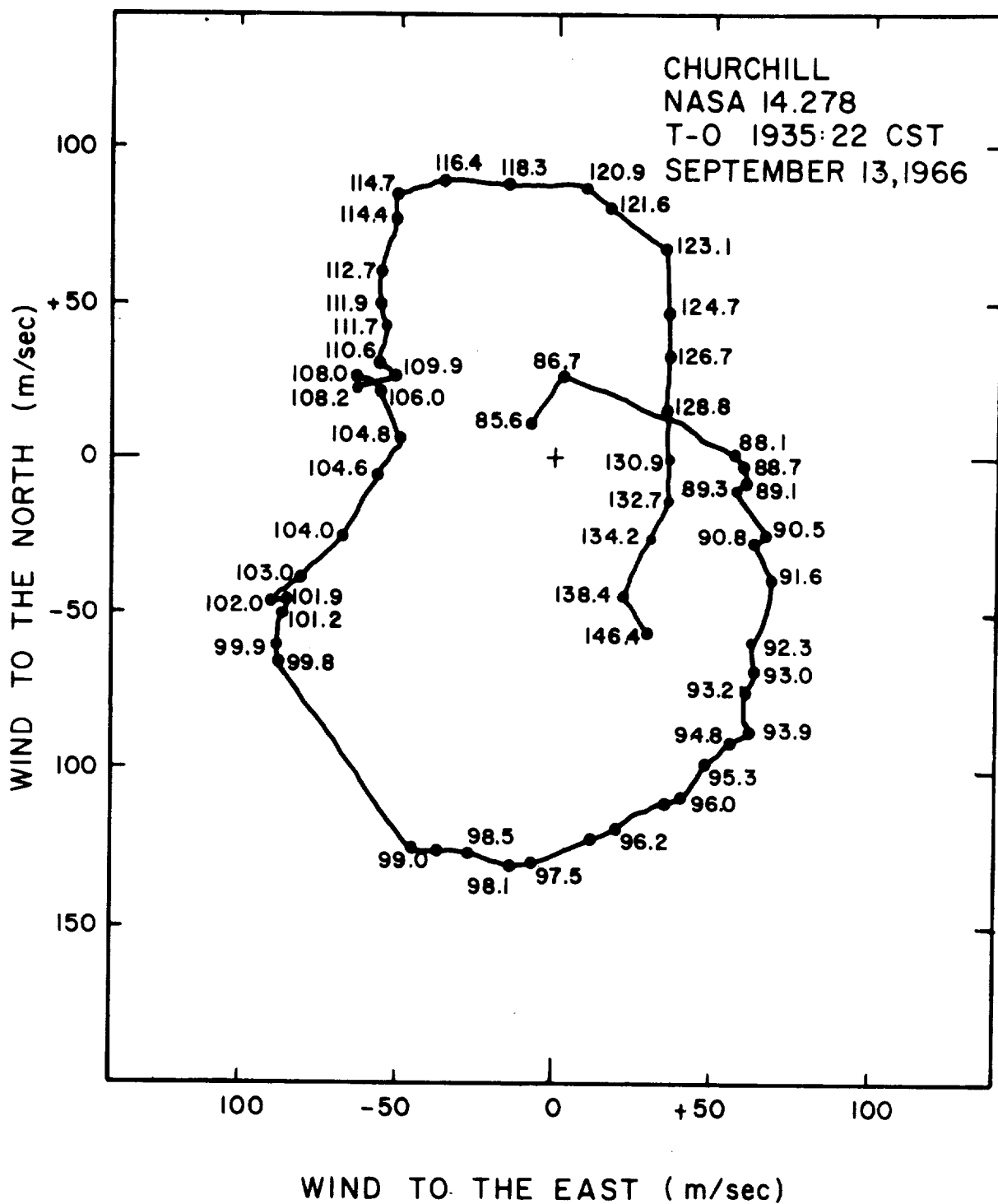
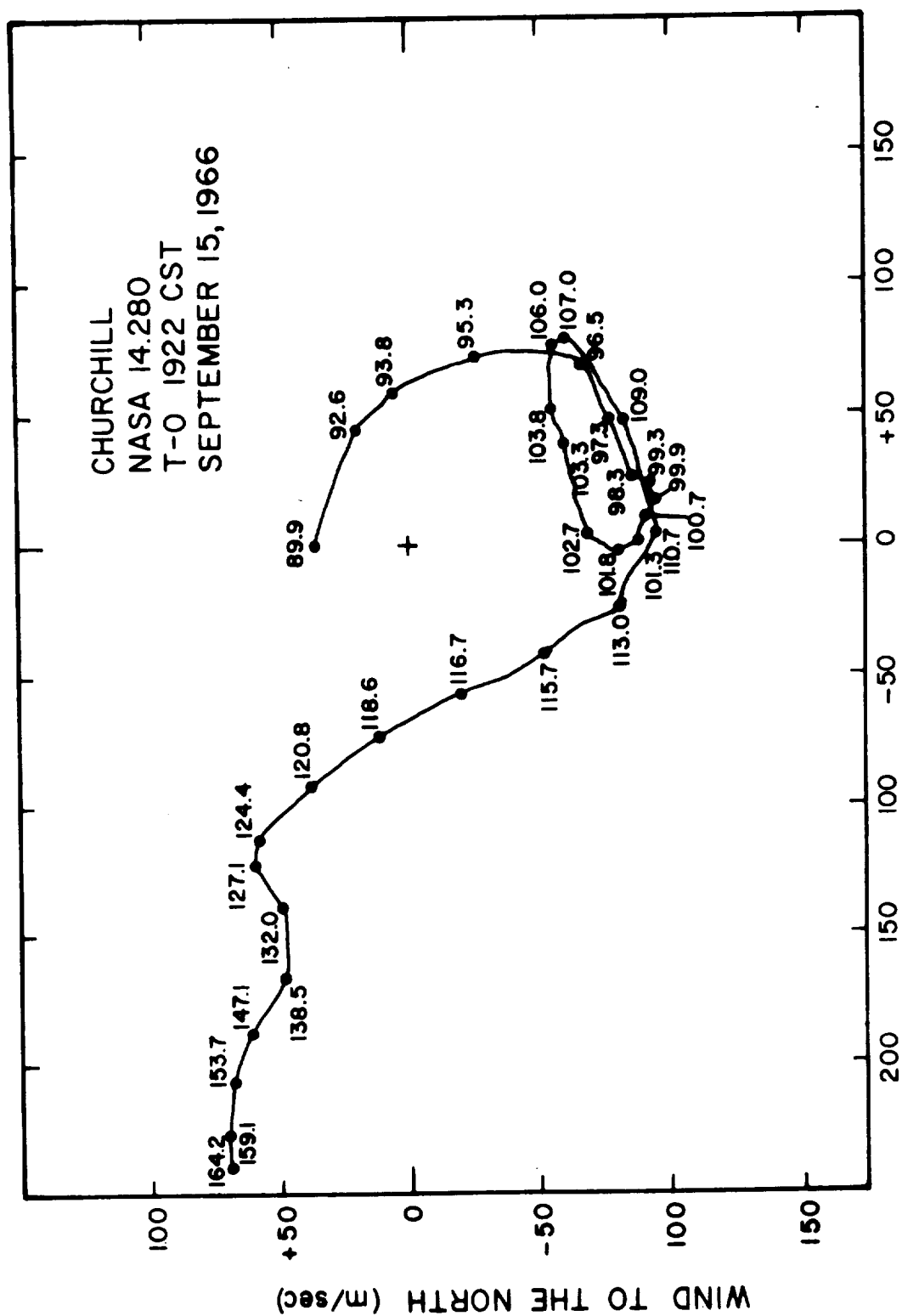


Figure 1. Wind hodograph, 13 September 1966, 1935:22 CST.



WIND TO THE EAST (m/sec)

Figure 2. Wind hodograph, 15 September 1966, 1922 CST.

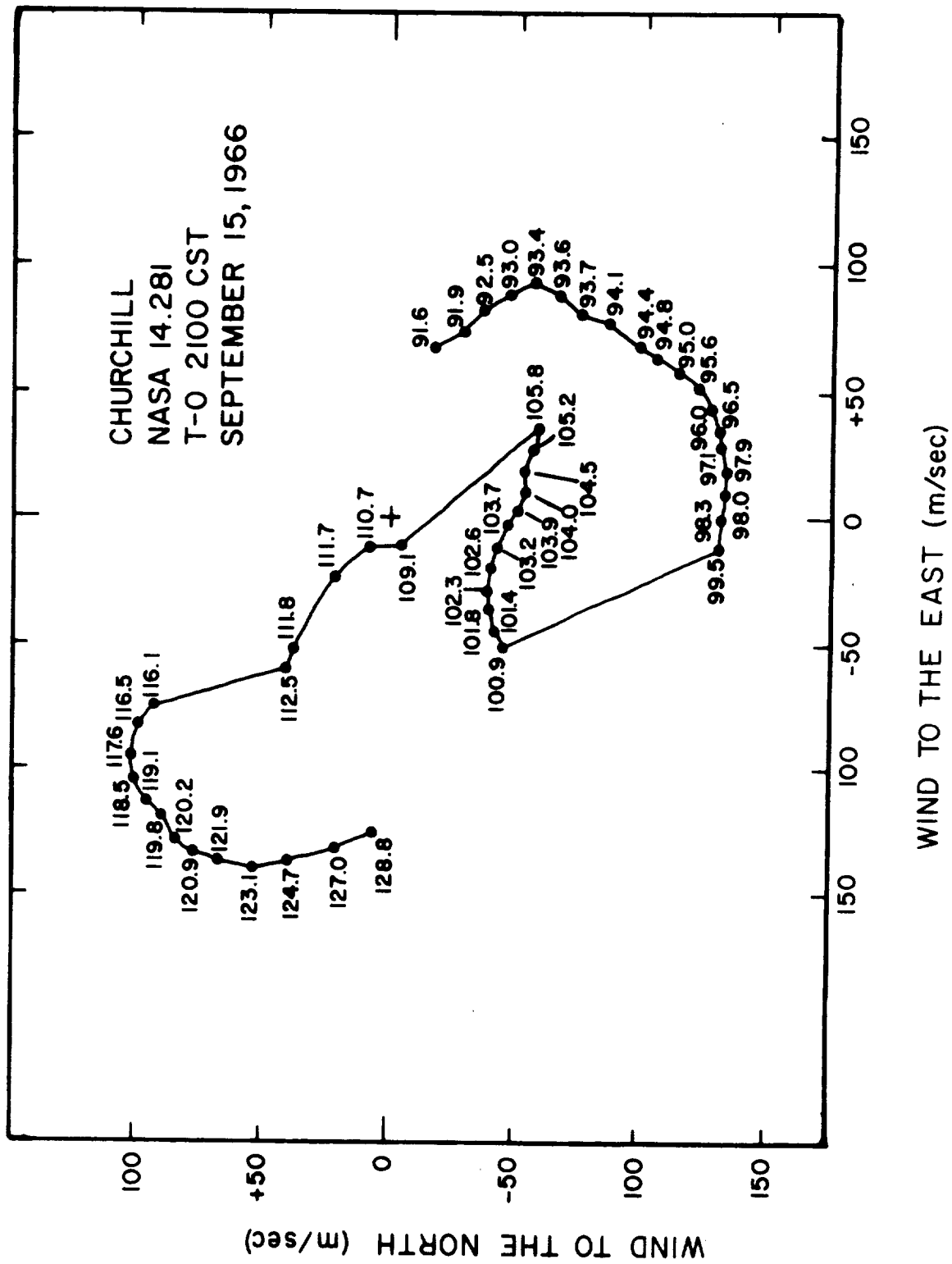
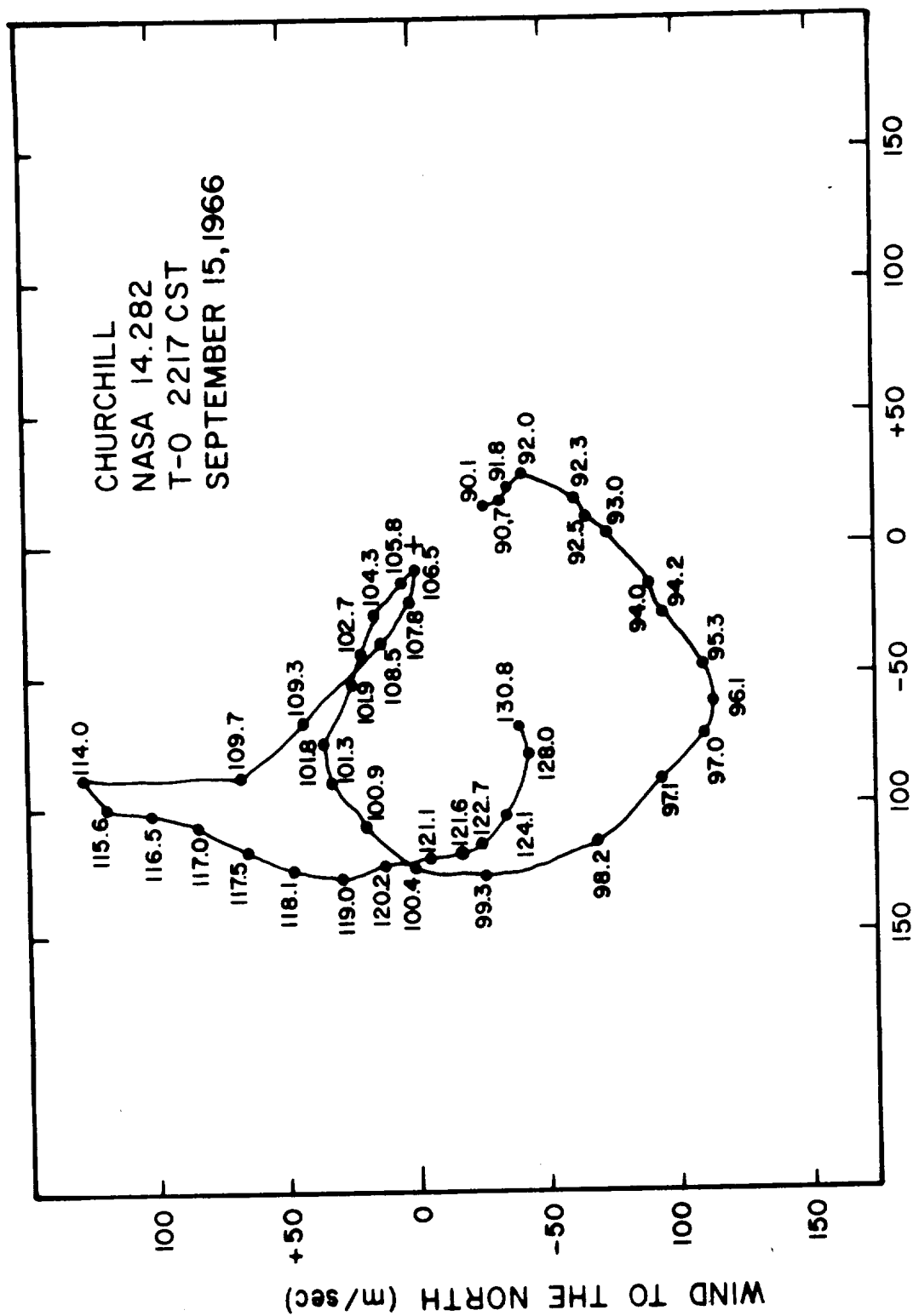


Figure 3. Wind hodograph, 15 September 1966, 2100 CST.



WIND TO THE EAST (m/sec)

Figure 4. Wind hodograph 15 September 1966, 2217 CST.

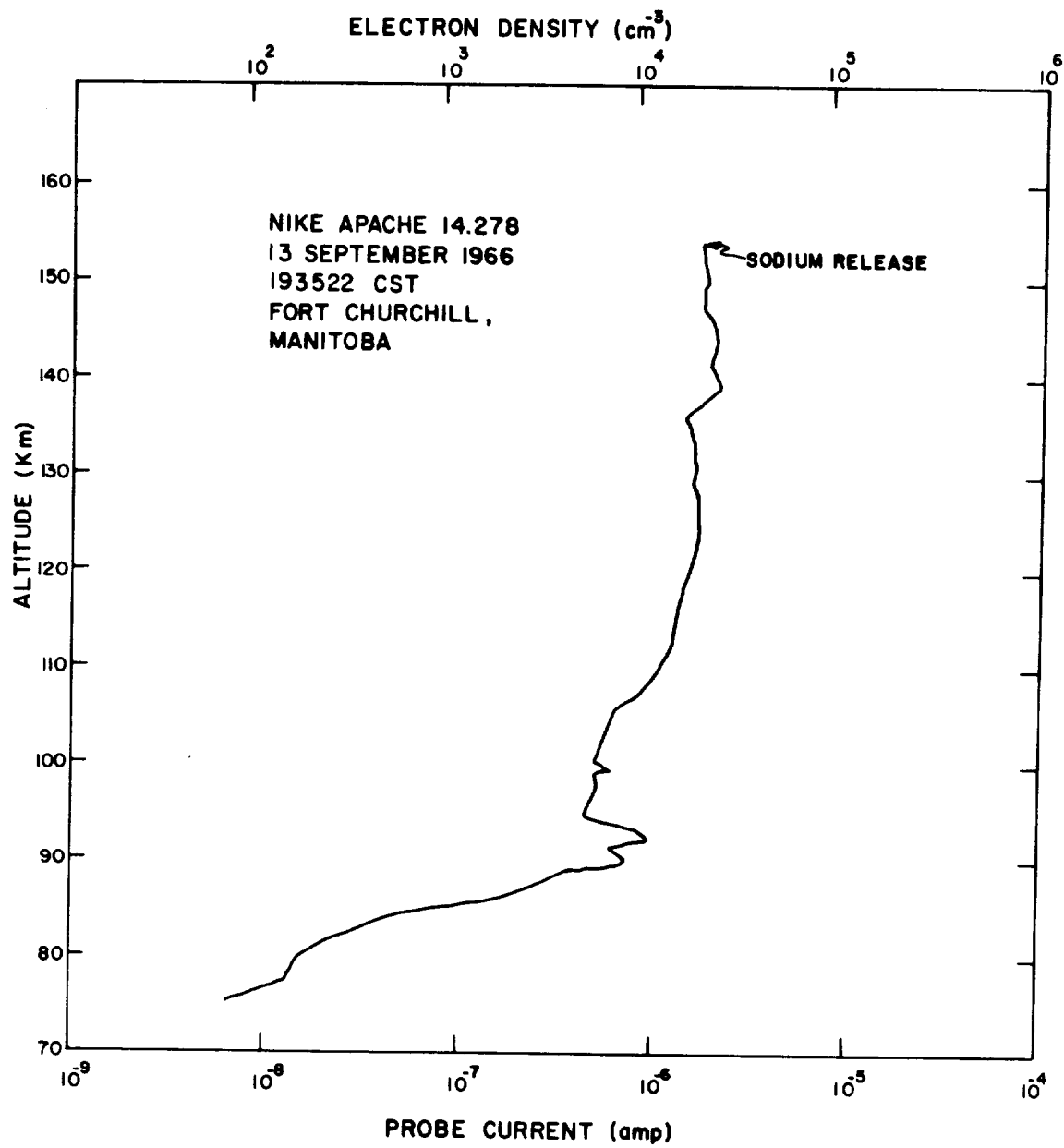


Figure 5. Electron density profile, 13 September 1966, 1935:22 CST.

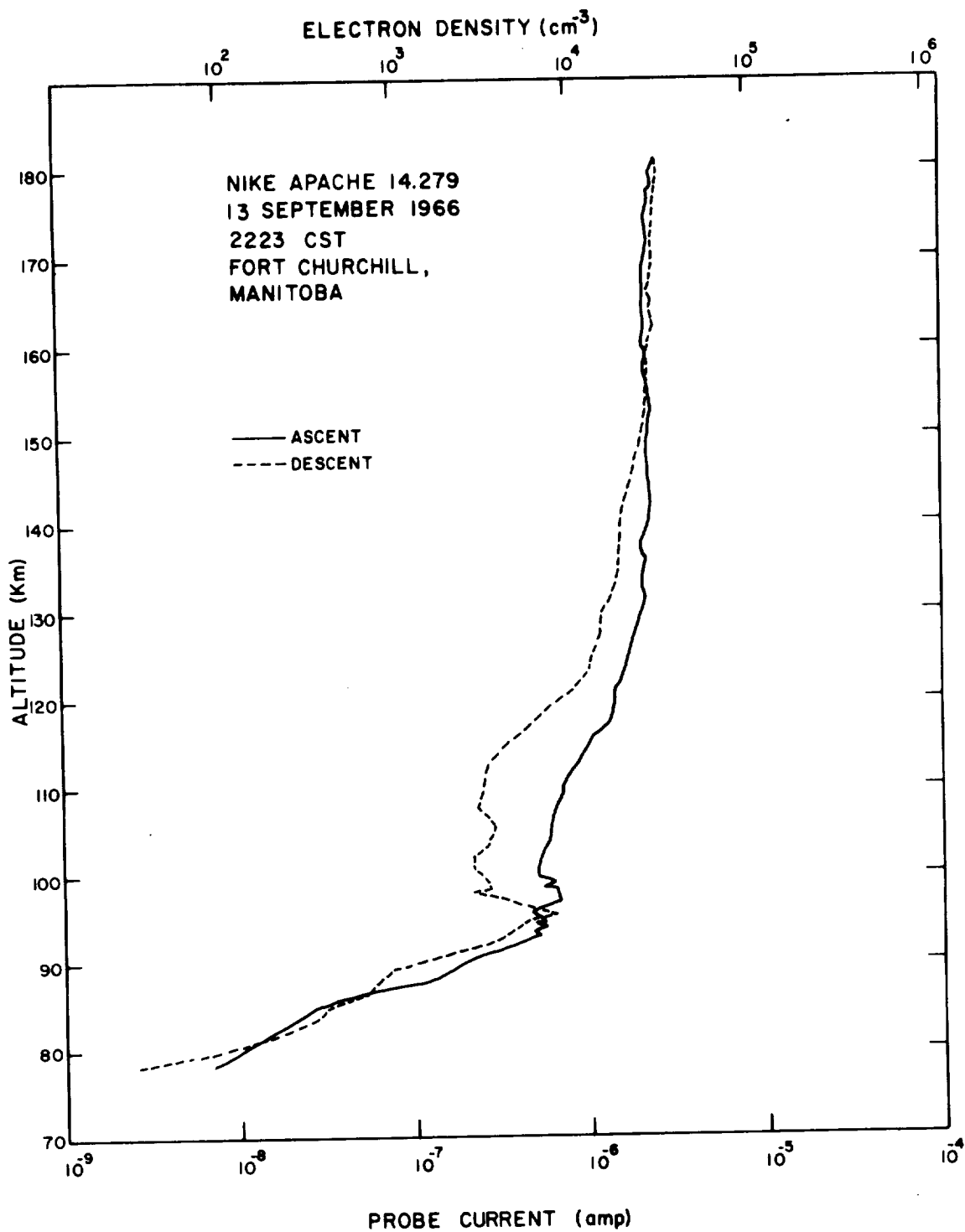


Figure 6. Electron density profile, 13 September 1966, 2223 CST.

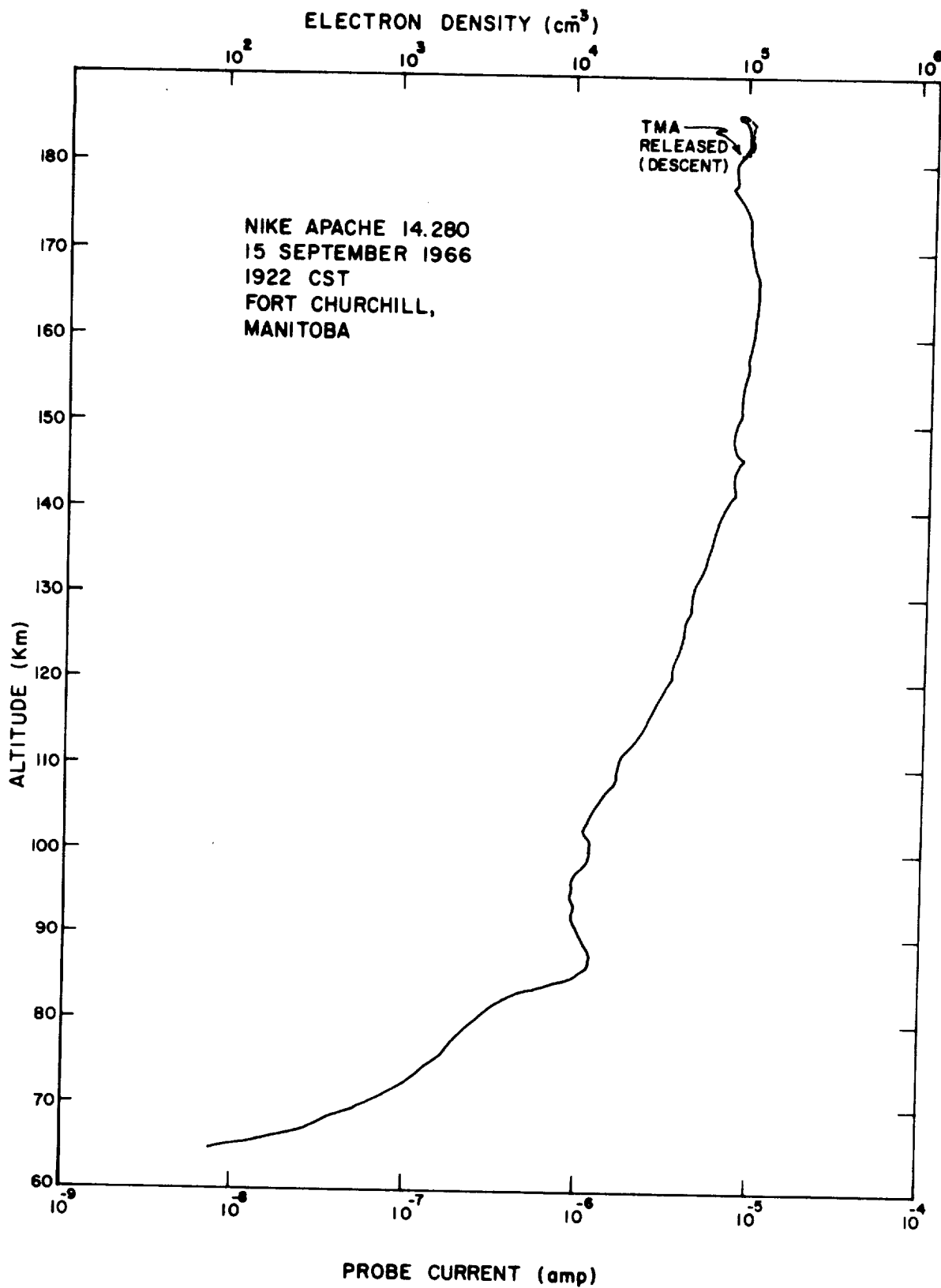


Figure 7. Electron density profile, 15 September 1966, 1922 CST.

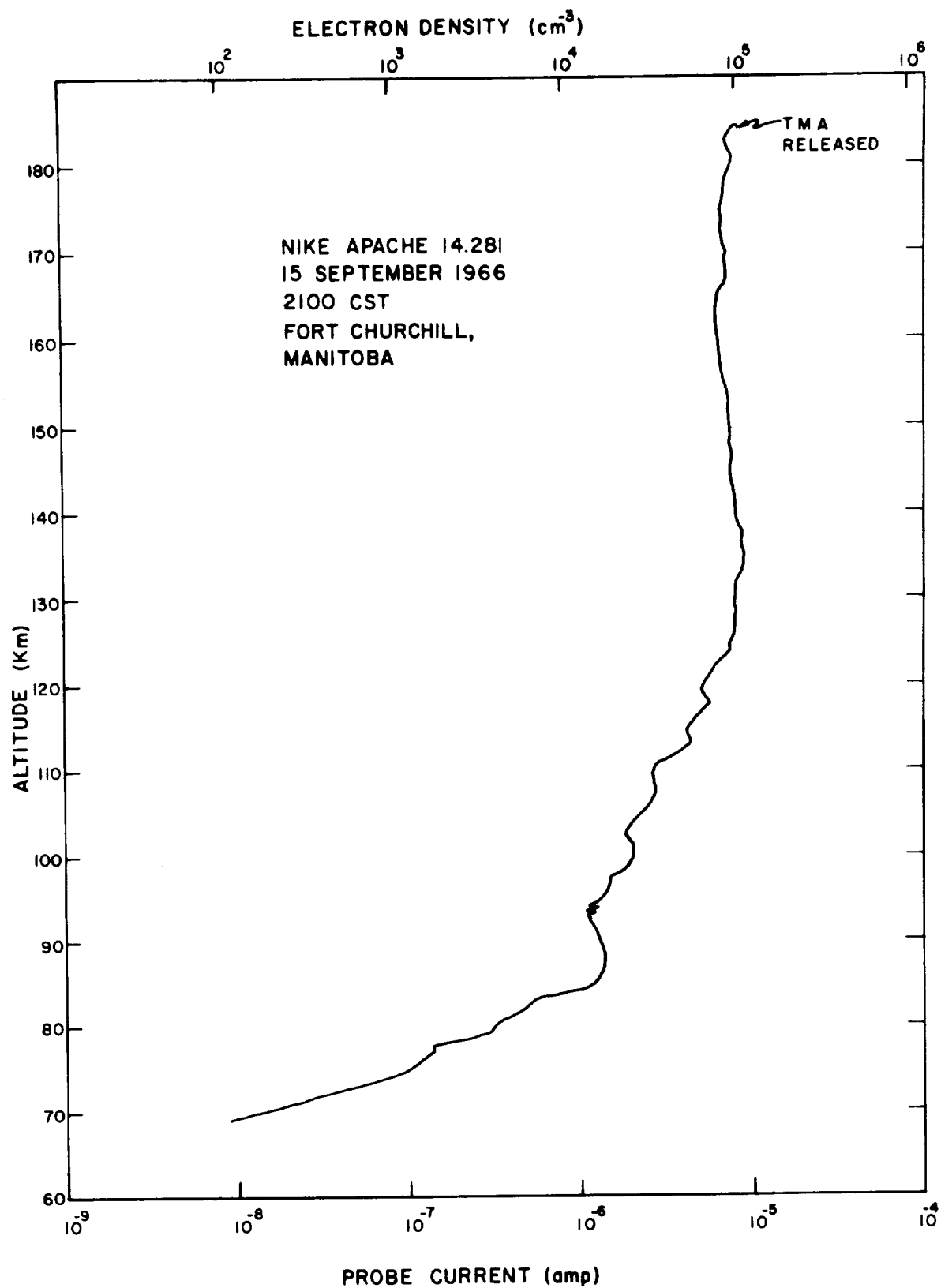


Figure 8. Electron density profile, 15 September 1966, 2100 CST.

density though differences in detail of structure can be seen. The two profiles on the night of 15-16 September 1966, separated by 108 minutes, similarly are in agreement with each other on magnitude though differing in detail of electron density. The electron density on this latter night was, however, significantly greater than on the earlier night, particularly in the D region (i.e. below 90 km). Whereas the electron densities on the earlier night are more typical of values seen, for example, at Wallops Island at night, those of the later night are indicative of disturbed conditions.

The profiles of both nights show in the E region a feature which distinguishes the auroral zone (i.e. Fort Churchill) data from the mid-latitude (i.e. Wallops Island) data. This is the absence at the high latitudes of a trough of electron density which occurs at lower latitudes in the altitude range about 130 to 150 km. There the electron density shows values one or two orders of magnitude lower than the peak values occurring between 95 and 120 km. The absence of the trough at high latitudes is attributed to the presence of an essentially continuous source of ionization, which is confirmed by the presence of faint auroras on each night.

AIRCRAFT OBSERVATIONS AT FORT CHURCHILL

Aircraft Flight Plan

Two experiments planned for the aircraft were a photographic one from the windows on the right side of the aircraft, and a photometric one from the windows on the left side. The photographic experiment was to be for approximately the first eight minutes after chemical release from the rocket. The flight plans (one for an up-trail release and one for a down-trail release) for this portion are shown in the sketch, Figure 9, with details given in Table 3.

TABLE 3

AIRCRAFT FLIGHT PLAN

	Up-Trail Plan	Down-Trail Plan
Aircraft Altitude	20,000 ft	20,000 ft
Aircraft Ground Speed	330 knots	330 knots
Initial Point	58°29' N 94°19' W at T+1 min	58°29' N 93°29' W at T+5 min
Heading - Leg A	330°T	330°T
Duration - Leg A	3 min	3 min
Right Turn	1 min duration	1 min duration
Heading - Leg B	30°T	30°T
Duration - Leg B	3 min	3 min
Right Turn	to heading 180°T	to heading 180°T

The two flight plans were identical except that the up-trail was displaced 48 km (25.9 nmi) to the west of the down-trail plan, and the time of arrival at the Initial Point (IP) was T+1 min (time from rocket launch) for the up-trail and T+5 min for the down-trail plan. Leg A was on a bearing of 330 degrees T, 330 knots ground speed, for a duration of three minutes from the IP. A one-minute right turn to a heading of 30 degrees T was to be made at approximately 4 km (2.2 nmi) east of the Launch Point (LP) (down-trail), or 44 km (23.7 nmi) west of the LP for the up-trail plan. Leg B was on a bearing of 30 degrees T, 330 knots ground speed, for a duration of three minutes from completion of the turn. At the end of this leg, seven minutes from the IP, a right turn to a heading of 180 degrees T took place so that the cloud would be visible from the left side of the aircraft for the photometric experiment. The flight at this time was to be directed by the project scientist so that a selected portion of the cloud would be kept in view for approximately a half-hour.

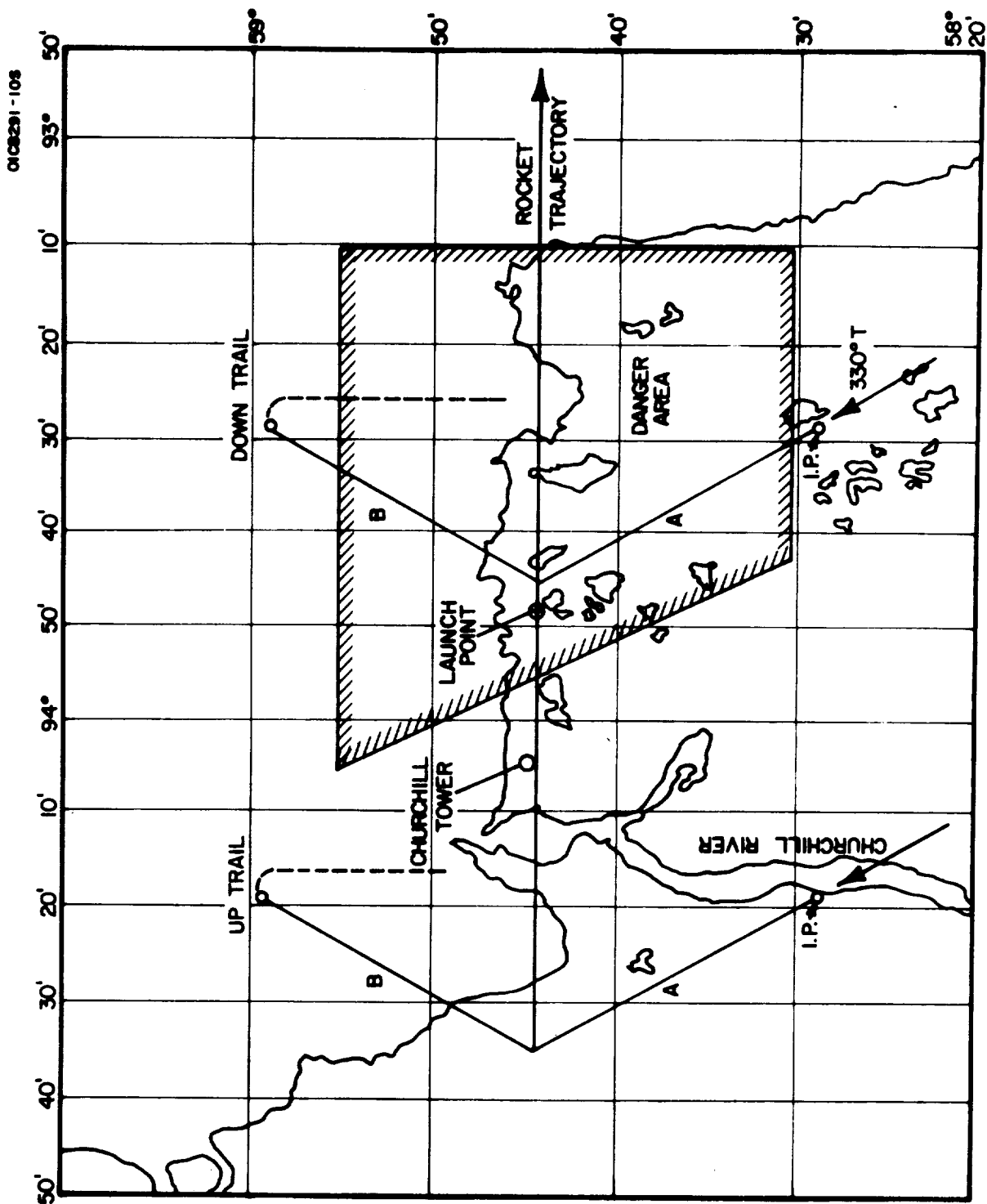


Figure 9. Flight plan.

The most important feature in the flight plan is the consistency of the heading and ground speed on Legs A and B, not the precise time of arrival at a geographic location or the exact duration of the Leg. In the event of a large deviation in the planned trajectory of the rocket, the project scientist would be able to request a new heading for a portion of the flight. Again it is important that once attained, the heading and ground speed must be as constant as possible.

Aircraft Operation

The four successful rocket releases were on the descent portion of the trajectory; therefore, the down-trail plan was flown on all flights. The only deviation from the aforementioned plan was at the end of Leg B on the flight for NASA 14.278. A left turn to a heading of 300 degrees T was made and the heading maintained for approximately six minutes. At this time a slow left turn was initiated to a heading of approximately 225 degrees T. The six-minute run increased the slant range to the upper portion of the cloud so that the fixed pointing angle of the French instrument would be accommodated. The 225-degree heading was varied in five and ten-degree increments in an attempt to locate the cloud in the narrow field of view of the French instrument. The Fastie spectrometer, with a larger field of view, was making continuous measurements during this portion of the flight.

Figures 10, 11, 12 and 13 are 70-mm photographs taken from the aircraft on flight 14.280 (TMA). Figures 10 and 11 were taken on Leg A and Figures 12 and 13 on Leg B. These photographs were taken with an aperture of 1.5, 1/10-sec exposure, on Kodak 2475 film, unfiltered. The sharpness of the star images (with stars of fourth magnitude easily visible at an 8-degree solar depression angle) shows that aircraft motion is not a problem for this exposure duration.

It was found that positioning the aircraft was more difficult for the night shots than it was for the twilight shots, due in part to the reduced intensity of the cloud and to the lower height at which the cloud becomes visible. Sixty-degree windows with a twenty-degree freedom in the elevation positioning of the camera would be advantageous for future aircraft trail photography.

Analytical Method

The problem under consideration is tracking a cloud of vapor (or of an identifiable point on a vapor trail) from a high-flying aircraft. The following assumptions are made (see Table 4 for the definition of symbols used in this discussion and in the following explanation of the data reduction methodology):

- (1) The cloud moves with a constant, horizontal velocity.
- (2) The flight of the aircraft consists of two legs. The height of the aircraft is the same for both legs. The horizontal velocity of the aircraft during each leg is arbitrary but constant.



Figure 10. Trail photographed from aircraft, 15 September 1966

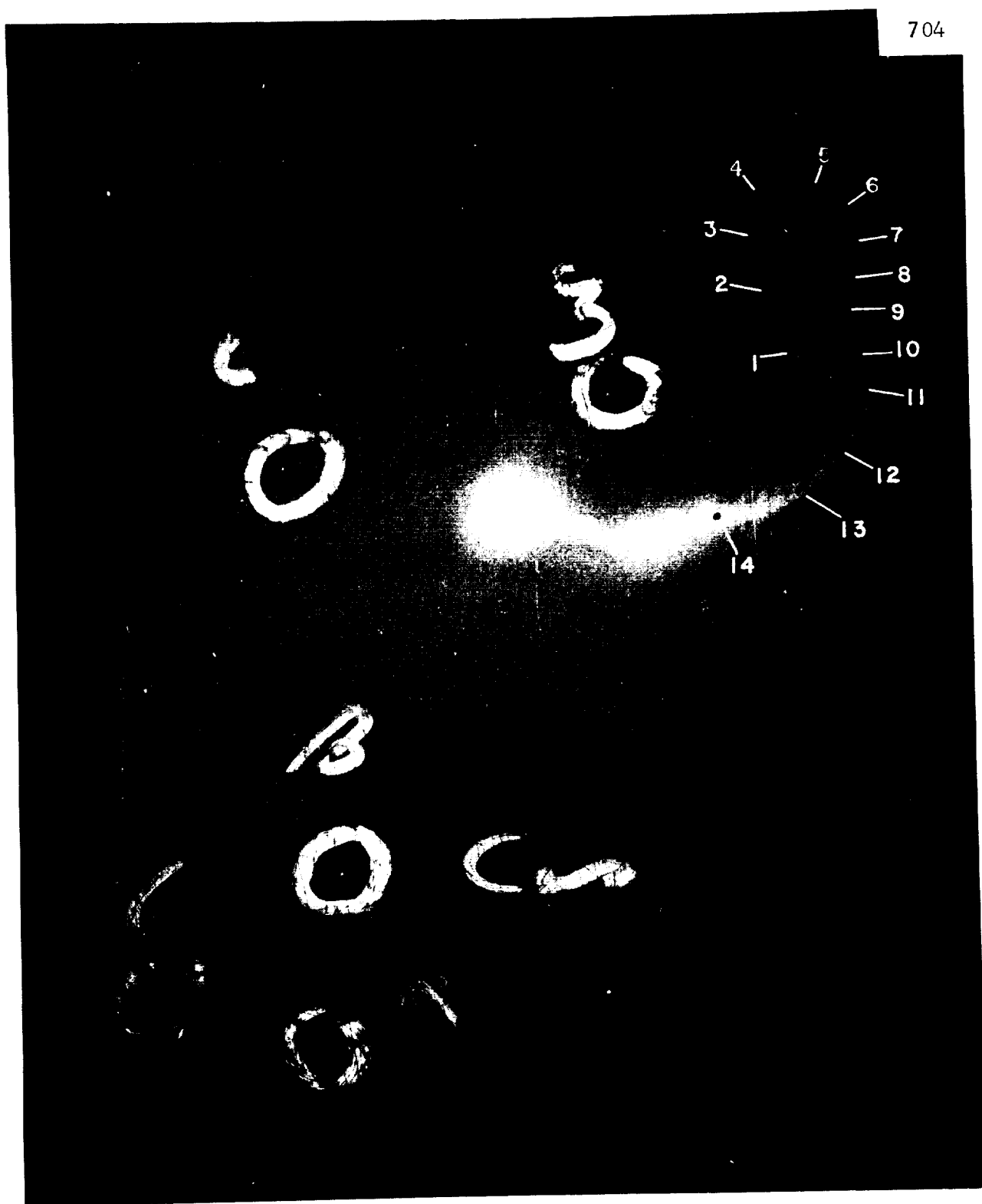


Figure 11. Trail photographed from aircraft, 15 September 1966

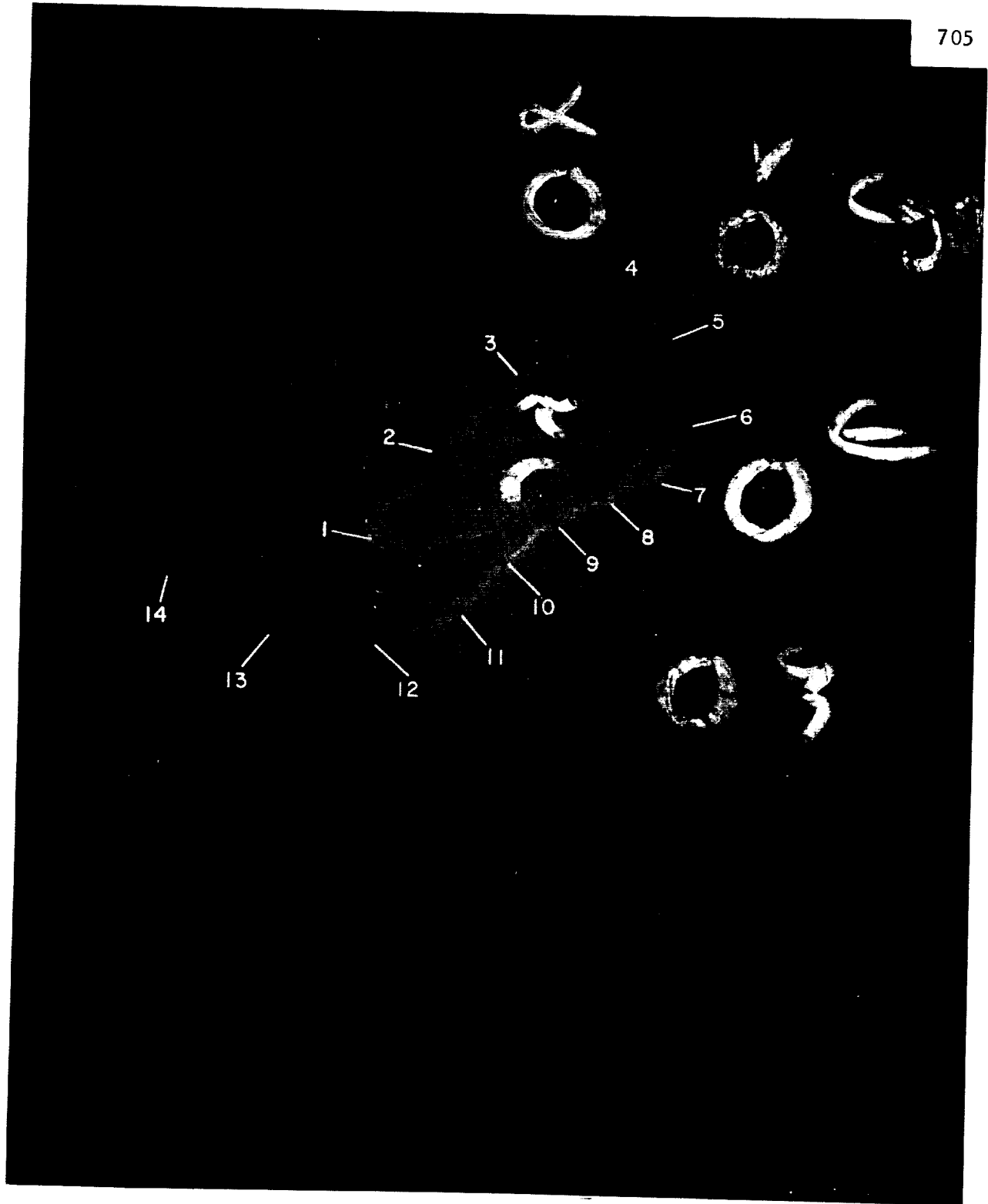


Figure 12. Trail photographed from aircraft, 15 September 1966

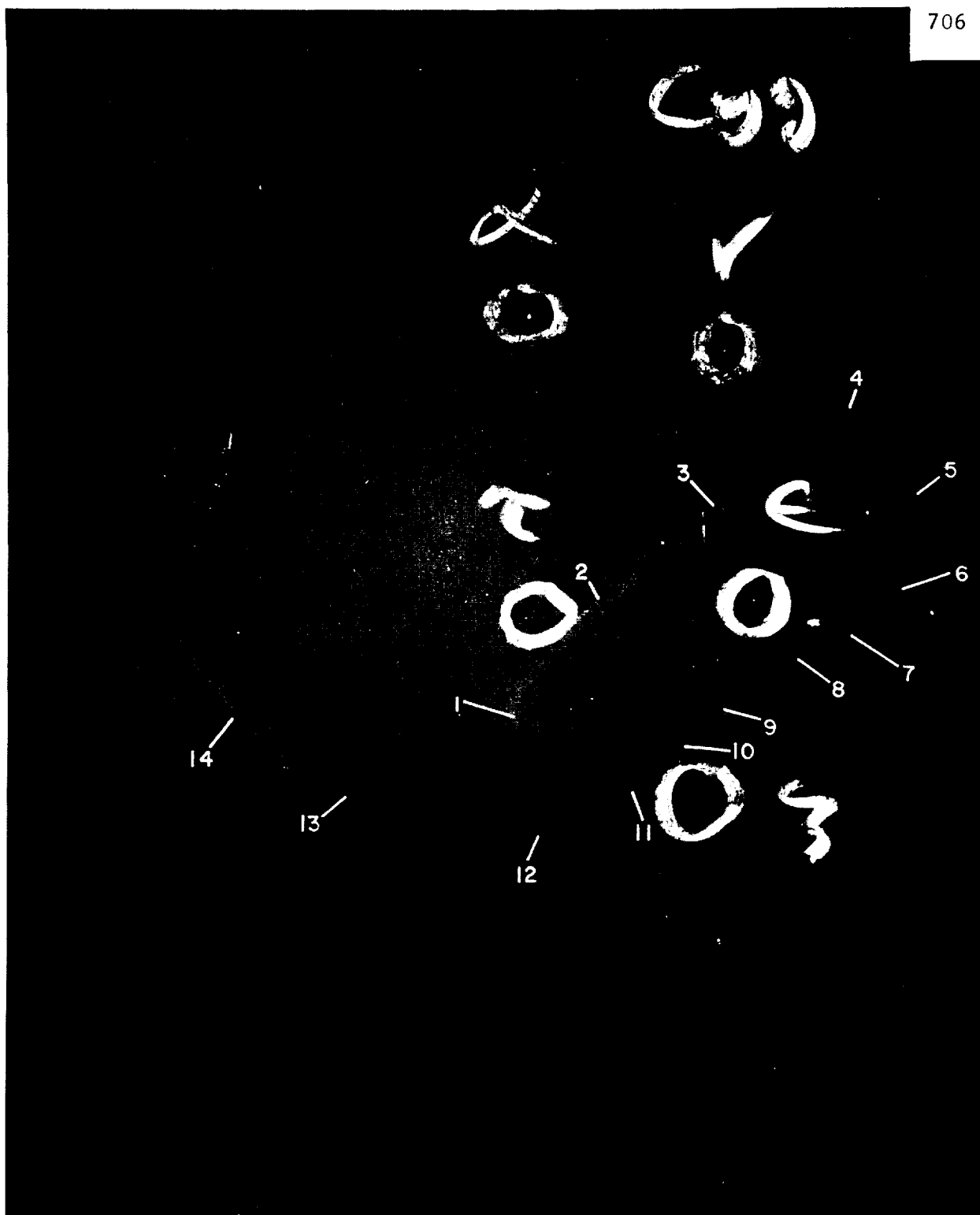


Figure 13. Trail photographed from aircraft, 15 September 1966

TABLE 4

SYMBOLS FOR THE ANALYTICAL METHOD AND DATA REDUCTION

Where quantities differ in the two legs of the flight,
a superscript identifies: (1) Leg A, (2) Leg B

$(U^{(1)}, U^{(2)})$	= speed of aircraft
$(H^{(1)}, H^{(2)})$	= heading of aircraft
$(x_a^{(1)}, y_a^{(1)}), (x_a^{(2)}, y_a^{(2)})$	= coordinates specifying position (real or extrapolated) of aircraft at $t = 0$
$(U_x^{(1)}, U_y^{(1)}), (U_x^{(2)}, U_y^{(2)})$	= components of aircraft velocity
(x_c, y_c)	= coordinates of cloud (real or extrapolated) at $t = 0$
(V_x, V_y)	= components of cloud velocity
$(X_a^{(1)}, Y_a^{(1)}), (X_a^{(2)}, Y_a^{(2)})$	= coordinates specifying instantaneous aircraft position
(X_c, Y_c)	= coordinates specifying instantaneous cloud position
$(X^{(1)}, Y^{(1)}), (X^{(2)}, Y^{(2)})$	= coordinates specifying instantaneous position of cloud relative to aircraft
$(\dot{X}^{(1)}, \dot{Y}^{(1)}), (\dot{X}^{(2)}, \dot{Y}^{(2)})$	= velocity components of cloud relative to aircraft
(A, E)	= azimuth and elevation angle of cloud as seen by observer on aircraft
$(X_o^{(1)}, Y_o^{(1)}), (X_o^{(2)}, Y_o^{(2)})$	= coordinates specifying position (real or extrapolated) of clouds relative to aircraft at $t = 0$
Z_a, Z_c	= height of aircraft and cloud, respectively
Z	= $Z_c - Z_a$

The directions of the x and y axes correspond to eastward and northward, respectively.

In Figure 14, $\underline{U}^{(1)}$ and $\underline{U}^{(2)}$ represent the velocity vectors of the aircraft during the first and the second leg of the flight, respectively. The angles $H^{(1)}$ and $H^{(2)}$ are the respective headings, measured from NORTH ($H=0$ degree) through EAST ($H=90$ degrees). Accordingly, the northward (U_y) and eastward (U_x) components of the aircraft velocity during the i th leg are given by the equations

$$U_x^{(i)} = U^{(i)} \sin H^{(i)}, \quad U_y^{(i)} = U^{(i)} \cos H^{(i)}$$

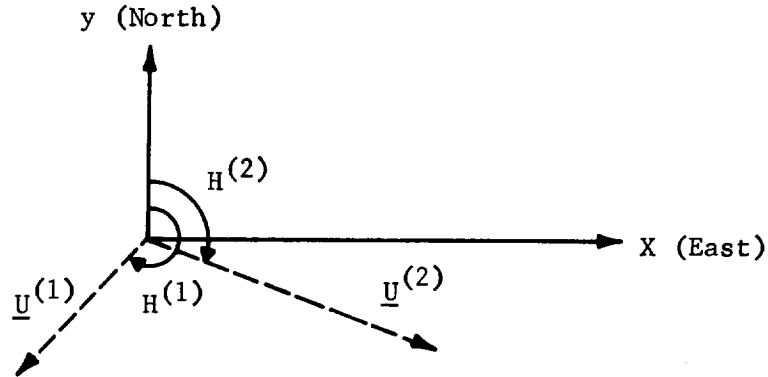


Figure 14.

The position of the aircraft at the time t is specified by the coordinates

$$x_a^{(i)}(t) = x_a^{(i)} + t U_x^{(i)}, \quad y_a^{(i)}(t) = y_a^{(i)} + t U_y^{(i)}$$

where $x_a^{(i)}$ and $y_a^{(i)}$ specify the position the aircraft would have occupied at the time $t = 0$ if it were following the i th leg of the flight at that time. An analogous set of equations specifies the position of the vapor cloud:

$$X_c(t) = x_c + tV_x, \quad Y_c(t) = y_c + tV_y$$

where V_x and V_y are the eastward and northward components of the cloud velocity, and x_c and y_c specify the position (real or extrapolated) of the cloud at the time $t = 0$. It is convenient to define the relative velocity components (of the cloud relative to the aircraft)

$$\dot{X}^{(i)} = V_x - U_x^{(i)}, \quad \dot{Y}^{(i)} = V_y - U_y^{(i)}$$

We also define the parameters

$$X_o^{(i)} = x_c - x_a^{(i)}, \quad Y_o^{(i)} = y_c - y_a^{(i)}$$

specifying the position of the cloud relative to the aircraft at the time $t = 0$. Then the position of the cloud relative to the aircraft is given by the equations

$$X^{(i)}(t) = X_c - X_a^{(i)} = X_o^{(i)} + t\dot{X}^{(i)}, \quad Y^{(i)}(t) = Y_c - Y_a^{(i)} = Y_o^{(i)} + t\dot{Y}^{(i)},$$

$$Z = Z_c - Z_a$$

where Z_c and Z_a are the fixed heights of the cloud and aircraft, respectively.

Let A and E be the azimuth and elevation angles of the cloud as measured by an observer on the aircraft.

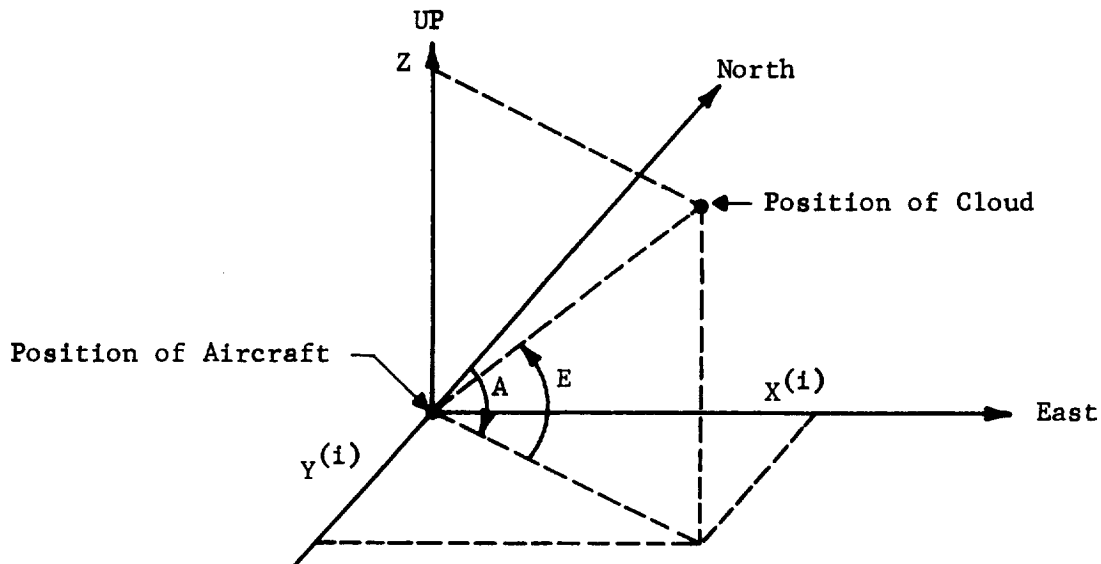


Figure 15.

Using Figure 15 we establish the relations

$$X^{(i)}(t) = Y^{(i)}(t) \tan A(t) \quad (1a)$$

$$X^{(i)}(t) = Z \sin A(t) \cot E(t) \quad (1b)$$

$$X^{(i)}(t) = Z \cos A(t) \cot E(t) \quad (1c)$$

Only two of these relations are independent.

Let us assume that a series of measurements of A and E are carried out at times t_1 , t_2 , and t_3 , all on the same leg of the flight. Then

$$X^{(i)}(t_1) = X_o^{(i)} + t_1 \dot{X}^{(i)} = Z F_x(t_1)$$

$$X^{(i)}(t_2) = X_o^{(i)} + t_2 \dot{X}^{(i)} = Z F_x(t_2)$$

$$X^{(i)}(t_3) = X_o^{(i)} + t_3 \dot{X}^{(i)} = Z F_x(t_3)$$

where

$$F_x(t) = \sin A(t) \cot E(t)$$

If we eliminate $X_o^{(i)}$ from the preceding equations, we have

$$(t_2 - t_1) \dot{X}^{(i)} = Z [F_x(t_2) - F_x(t_1)]$$

$$(t_3 - t_2) \dot{X}^{(i)} = Z [F_x(t_3) - F_x(t_2)]$$

This system of equations does not have a unique solution. In order that any solution exist, however, it is necessary that

$$(t_2 - t_1) [F_x(t_3) - F_x(t_2)] - (t_3 - t_2) [F_x(t_2) - F_x(t_1)] = 0$$

If we had used Equation (1c), we would have obtained three relations of the form

$$Y^{(1)}(t) = Y_o^{(1)} + t \dot{Y}^{(1)} = Z F_y(t)$$

$$\text{for } t = t_1, t_2, \text{ and } t_3$$

where

$$F_y(t) = \cos A(t) \cot E(t)$$

The requirement that a solution exists would then have led to the equation

$$(t_2 - t_1) [F_y(t_3) - F_y(t_2)] - (t_3 - t_2) [F_y(t_2) - F_y(t_1)] = 0$$

These relations can be generalized to

$$(t_j - t_i) [F_x(t_k) - F_x(t_j)] - (t_k - t_j) [F_x(t_j) - F_x(t_i)] = 0$$

and

$$(t_j - t_i) [F_y(t_k) - F_y(t_j)] - (t_k - t_i) [F_y(t_j) - F_y(t_i)] = 0$$

where t_i , t_j , and t_k are any three times pertaining to the same leg of the flight. These relations are useful for checking the self-consistency of the data.

In order to determine all the quantities of interest, we need information from two different times from each leg of the flight. Let us suppose, then, that A and E are measured at the times t_{m1} and t_{m2} during the first leg, and t_{n1} and t_{n2} during the second. The appropriate equations are

$$X_o^{(1)} + t_{m1} \dot{X}^{(1)} = Z F_x(t_{m1}), \quad Y_o^{(1)} + t_{m1} \dot{Y}^{(1)} = Z F_y(t_{m1}),$$

$$X_o^{(1)} + t_{m2} \dot{X}^{(1)} = Z F_x(t_{m2}), \quad Y_o^{(1)} + t_{m2} \dot{Y}^{(1)} = Z F_y(t_{m2}),$$

$$X_o^{(2)} + t_{n1} \dot{X}^{(2)} = Z F_x(t_{n1}), \quad Y_o^{(2)} + t_{n1} \dot{Y}^{(2)} = Z F_y(t_{n1}),$$

$$X_o^{(2)} + t_{n2} \dot{X}^{(2)} = Z F_x(t_{n2}), \quad Y_o^{(2)} + t_{n2} \dot{Y}^{(2)} = Z F_y(t_{n2})$$

We can proceed to the solution by using the equations in either the first (X) or the second (Y) column. Elimination of $X_o^{(1)}$, $X_o^{(2)}$, $Y_o^{(1)}$, and $Y_o^{(2)}$ gives

$$\begin{aligned} \dot{X}^{(1)} &= Z G_x(t_{m2}, t_{m1}), \quad \dot{Y}^{(1)} = Z G_y(t_{m2}, t_{m1}), \\ \dot{X}^{(2)} &= Z G_x(t_{n2}, t_{n1}), \quad \dot{Y}^{(2)} = Z G_y(t_{n2}, t_{n1}) \end{aligned} \quad (2)$$

where

$$G_x(t, t') = [F_x(t) - F_x(t')]/(t - t'), \quad G_y(t, t') = [F_y(t) - F_y(t')]/(t - t')$$

Remembering the relations

$$\dot{X}^{(1)} = V_x - U_x^{(1)}, \quad \dot{X}^{(2)} = V_x - U_x^{(2)}$$

$$\dot{Y}^{(1)} = V_y - U_y^{(1)}, \quad \dot{Y}^{(2)} = V_y - U_y^{(2)}$$

we see that the four equations (Eq. (2)) contain the three unknowns Z , V_x , and V_y . Hence there is redundant information. From the X-column we have

$$Z [G_x(t_{n2}, t_{n1}) - G_x(t_{m2}, t_{m1})] = \dot{X}^{(2)} - \dot{X}^{(1)}$$

or

$$Z = (U_x^{(1)} - U_x^{(2)})/[G_x(t_{n2}, t_{n1}) - G_x(t_{m2}, t_{m1})]$$

Similarly, from the Y-column we obtain the result

$$Z = (U_y^{(1)} - U_y^{(2)})/[G_y(t_{n2}, t_{n1}) - G_y(t_{m2}, t_{m1})]$$

Because the measurements contain errors, the values of Z obtained from the two formulae will, in general, be different. Let Z represent the optimum choice,

obtained in some manner from the two different values. Corresponding to this choice, the optimally determined values of the other unknown quantities are:

$$\begin{aligned}\bar{V}_x &= \frac{1}{2} (U_x^{(1)} + U_x^{(2)}) + \frac{1}{2} \bar{Z} [G_x(t_{m2}, t_{m1}) + G_x(t_{n2}, t_{n1})], \\ \bar{V}_y &= \frac{1}{2} (U_y^{(1)} + U_y^{(2)}) + \frac{1}{2} \bar{Z} [G_y(t_{m2}, t_{m1}) + G_y(t_{n2}, t_{n1})], \\ \dot{\bar{X}}^{(1)} &= \bar{V}_x - U_x^{(1)}, \quad \dot{\bar{X}}^{(2)} = \bar{V}_x - U_x^{(2)}, \\ \dot{\bar{Y}}^{(1)} &= \bar{V}_y - U_y^{(1)}, \quad \dot{\bar{Y}}^{(2)} = \bar{V}_y - U_y^{(2)}, \\ \bar{X}_o^{(1)} &= \frac{1}{2} \bar{Z} [F_x(t_{m1}) + F_x(t_{m2})] - \frac{1}{2} \dot{\bar{X}}^{(1)} (t_{m1} + t_{m2}), \\ \bar{X}_o^{(2)} &= \frac{1}{2} \bar{Z} [F_x(t_{n1}) + F_x(t_{n2})] - \frac{1}{2} \dot{\bar{X}}^{(2)} (t_{n1} + t_{n2}), \\ \bar{Y}_o^{(1)} &= \frac{1}{2} \bar{Z} [F_y(t_{m1}) + F_y(t_{m2})] - \frac{1}{2} \dot{\bar{Y}}^{(1)} (t_{m1} + t_{m2}), \\ \bar{Y}_o^{(2)} &= \frac{1}{2} \bar{Z} [F_y(t_{n1}) + F_y(t_{n2})] - \frac{1}{2} \dot{\bar{Y}}^{(2)} (t_{n1} + t_{n2}), \\ \bar{x}_c &= \frac{1}{2} (x_a^{(1)} + x_a^{(2)} + \bar{X}^{(1)} + \bar{X}^{(2)}), \quad \bar{y}_c = \frac{1}{2} (y_a^{(1)} + y_a^{(2)} + \bar{Y}^{(1)} + \bar{Y}^{(2)}),\end{aligned}$$

Reduction of Data from Aircraft

The trail released by NASA 14.280 was photographed from the NASA research aircraft. This section contains the results of the analysis of the data, as well as a discussion of the accuracy of the results. Photographs obtained from other trails in the series have not been analyzed principally because of uncertainty in the aircraft position and heading.

Figures 10, 11, 12, and 13 are photographs of the trail corresponding to the times t_1 , t_2 , t_3 , and t_4 . The first two of these photographs were taken during the first leg of the flight, whereas the latter two photographs were taken during the second leg. On each photograph, points on the vapor trail have been designated by the numerals 1 through 14. The same numeral is used to designate a particular point on the trail in all four photographs. In addition, each photograph shows the stars used for calibration purposes.

The data pertaining to each point were analyzed separately; that is, each numbered point on the trail was treated independently. The information

available for each trail point consists of a pair of values $A(t)$ and $E(t)$, specifying the azimuth and elevation angles of the trail point with respect to the aircraft, for each of the four times t_1 , t_2 , t_3 and t_4 . This information, together with a knowledge of the aircraft velocity during the two legs of the flight, leads to the determination of the height Z_c , and the eastward (V_x) and northward (V_y) velocity components of the cloud. The formulae used for the calculation are listed at the end of the preceding section.

The wind hodograph derived from the analysis of the aircraft photographs is plotted in Figure 16. For comparison, the wind hodograph derived from the ground-based observations is plotted in the same figure. The agreement between the two hodographs is generally satisfactory. The aircraft data, however, are unsatisfactory in one important respect: they do not permit a sufficiently accurate determination of heights. This shortcoming is by no means inherent in the method of observation. Rather, it is a result of inaccuracies in timing, of the (relatively) slow speed of the aircraft used, and of the geometrical limitation of the windows of the aircraft.

The timers used for this experiment derived their electrical power from the aircraft's generator. The time of the first photograph taken is accurately known, but the time of subsequent photographs is accurate only to the extent that the timer was accurate. A check, during the flight, of the timer operation against a mechanical stopwatch revealed the timer to be randomly in error by almost 10 percent. A systematic error was also detected in and eliminated from the data.

This error can be avoided by the use of a timer that is insensitive to the range of fluctuations in voltage and frequency of the aircraft generator. For one of the cameras operated from the aircraft every fifth picture was accurately timed by the mechanical stopwatch. Unfortunately the exposure time used with this camera was too long, and the photographs were blurred by the vibration of the aircraft.

The second major source of error in the data is due to the limited speed of the aircraft, and to the geometrical limitations of the aircraft windows. The maximum length of each leg of the flight was determined by the requirements (1) that there be two legs of approximately equal duration, and (2) that the trail be visible through the existing windows. Given these conditions, less than three minutes were available for each leg. The photographs used in the present analysis were safely within this time interval, and separated by one minute during each leg. During this time the aircraft moved through less than 10 km. For such a distance the differences in the quantities used in the analysis were of the order of 10 percent so that there was a loss through subtraction of the first significant figure during the analysis. Thus a 1 percent error in the original data becomes a 10 percent error in the calculated height, much too large to be acceptable. It should be noted that an aircraft with, say, twice the speed of the aircraft used, would more than double the accuracy of the results, owing to the fact that such an aircraft would fly roughly twice as far away from the trail. This would reduce the

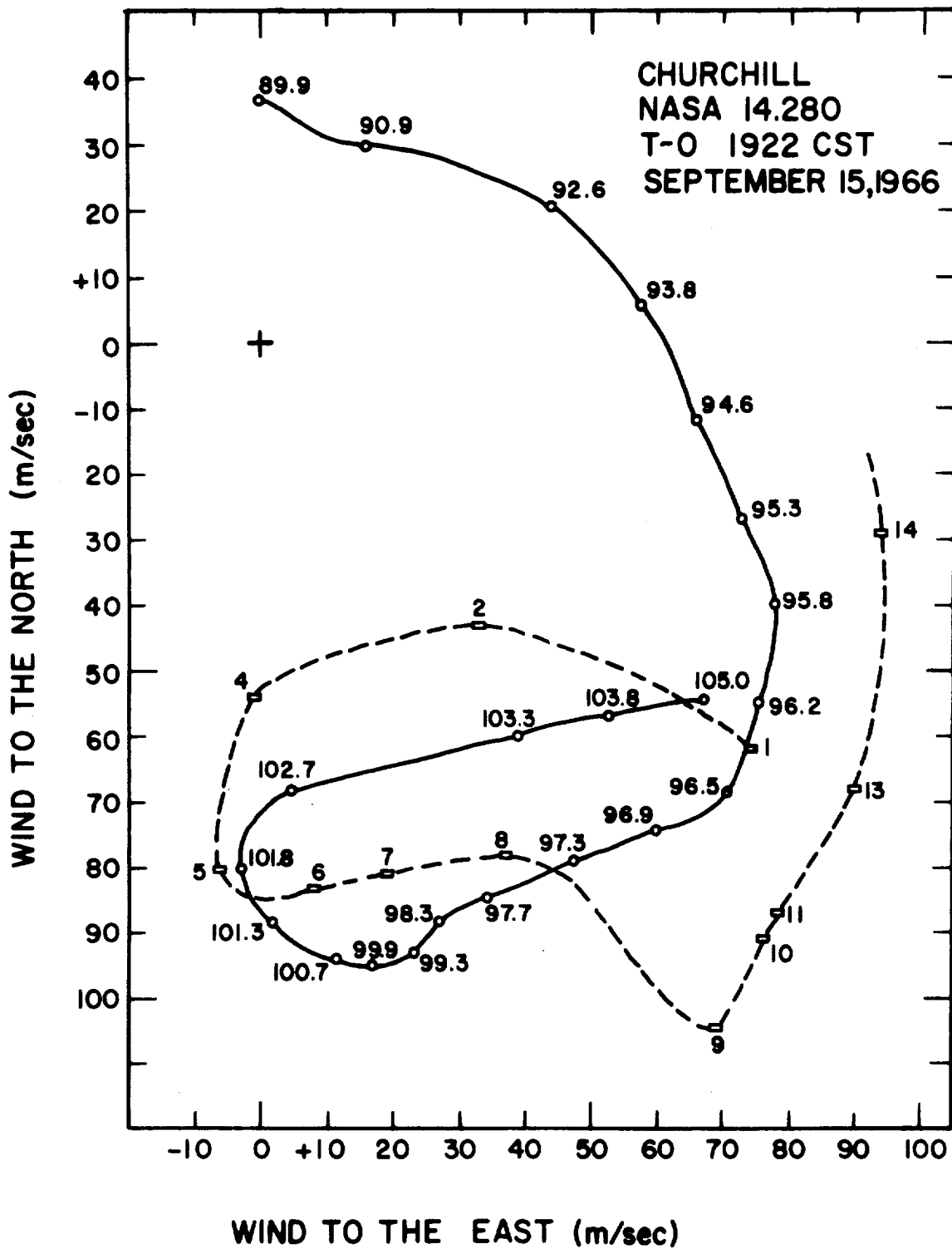


Figure 16. Wind hodographs 15 September 1966, 1922 CST.

elevation angle, and thus increase the rate of change of the quantities $\cot E \sin A$ and $\cot E \cos A$ that appear in the calculation.

A comparison of the hodographs of Figure 16 seems to indicate that they are rotated with respect to each other. This systematic difference may be due to inaccurate information concerning the aircraft's headings and speeds. A comparison of the aircraft-to-air with the aircraft-to-ground values of the speed and heading of the aircraft yields the air-to-ground speed and direction. Two such calculations are possible, one for each leg of the flight. The results are self-consistent only to within 10 percent. Further, the headings provided by the local radar installation were off by 90 degrees in one instance. There is, therefore, some unfortunate uncertainty associated with the flight path of the aircraft.

The preceding comments apply to the straightforward analysis of each trail point separately (as if it were an isolated cloud) and from the minimum required information (i.e., four photographs). A more complex method of analysis, utilizing the continuous nature of the trail, and the data from more than the minimum set of photographs, would improve the accuracy.

UPPER ATMOSPHERE TEMPERATURES DEDUCED FROM OBSERVATIONS OF AN AlO TRAIL AT TWILIGHT

Introduction

Only one trail of aluminum monoxide has been laid at twilight in the period covered by this report; however, considerable attention has been given to the method of analysis. The results of this investigation are detailed in GCA Technical Report 67-7-N. The conclusions reached will be summarized here. The definitions of symbols used for the AlO calculations are given in Table 5.

TABLE 5
SYMBOLS USED FOR AlO CALCULATIONS

Symbol	Description
S	Transition strength
ψ	Wave function
R_e	Electronic transition moment
r	r-centroid
v', v''	Vibrational quantum numbers at upper and lower and of transition
P	Vibrational transition probability
q	Franck-Condon Factor
θ	Angle between grating normal and spectrometer axis

The method of analysis consists of assigning to the vibrational and rotational levels of the AlO molecule a population distribution which is assumed to be determined by the Maxwell-Boltzmann distribution law. The relative intensity of solar irradiation at wavelengths corresponding to transitions among these levels is also required. With a knowledge of the relative transition probabilities, we may then calculate the rate of population of each vibrational and rotational level of the excited electronic state of AlO . At equilibrium, the rate of population of each level by absorption of solar radiation will be equal to the rate of depopulation by spontaneous radiation. Thus it is in theory possible to calculate synthetic spectra (relative intensities of emission lines or bands) corresponding to any assumed initial temperature.

Obviously the vibrational and rotational energy levels of the ground ($X^2\Sigma$) and first excited ($A^2\Sigma$) electronic states, the relative probabilities of transitions among these levels and the relative intensity of solar radiation at wavelengths corresponding to these transitions require to be well known.

Energy Levels of $A^2\Sigma$ and $X^2\Sigma$ States of AlO

Since considerable attention has been given to the AlO spectrum in various laboratories the wavelengths of the transitions are known to a high degree of precision. The molecular constants involved have been tabulated by Tyte and Nicholls [8]. Sharma [9] used the data to investigate the departure of the potential energy curves from Morse potential functions, and calculated corresponding vibrational wave function overlap integrals [10].

Relative Vibrational Transition Probabilities

To a first approximation the relative band strengths for transitions between two vibrational levels v' and v'' (of the $A^2\Sigma$ and $X^2\Sigma$ states, respectively) are given as

$$S_{v',v''} = \left| \int \psi_{v'} R_e(r) \psi_{v''} dr \right|^2$$

$$= R_e^2 \left[\int \psi_{v'} \psi_{v''} dr \right]^2$$

where $\left[\int \psi_{v'} \psi_{v''} dr \right]^2$ is known as the Franck-Condon factor and is abbreviated to $q_{v',v''}$. The electronic transition moment R_e is assumed to be fairly constant, so that the vibrational transition probabilities depend principally on the Franck-Condon factors.

When relative intensities have been measured in the laboratory it is observed that R_e can no longer be regarded as a constant for each electronic transition. It is generally assumed [11] that R_e varies as a function of \bar{r} the r -centroid, defined as

$$\bar{r} = \frac{\int \psi_{v'}(r) \psi_{v''} dr}{\int \psi_{v'} \psi_{v''} dr}$$

and the variation of R_e with (\bar{r}) has been determined for several aeronomically important constituents [12]. In the case of A_2O , however, there is a disagreement between the results of Hebert and Tyte [13,14] and the results of Tawde and Korwar [15,16]. The former obtain, from spectra excited by several different sources, a variation of the form,

$$R_e(r) = \text{const} (1 - 0.46 \bar{r})$$

using integrated band intensities, whereas the latter obtain

$$R_e(r) = \text{const} (1 - 1.093 \bar{r})$$

using integrated band intensities, and

$$R_e(r) = \text{const} (1 - 0.457 \bar{r})$$

using peak intensities.

In both cases considerable smoothing of the data was used to obtain these functions. It is pointed out here that the data used in the analyses failed to respond to a test for constant relative band intensities in any v'' progression. In other words, once a certain level v' has been populated by any excitation process, the relative intensities of emission bands originating in this level should be independent of the manner in which the v' level was populated. Therefore neither function $R_e(r)$ may be regarded as conclusive. Possible causes of this discrepancy include optical thickness of one or more emission bands and distortion of the molecular potentials by electric fields or high pressures. Tyte [17] found a variation of band strength with current density in the Nitrogen Second Positive System excited in a dc discharge.

There is excellent agreement on the values of the Frank-Condon factors and r -centroids. Franck-Condon factors were calculated by Nicholls [18] and by Tawde and Korwar [19] by different methods, both based on the assumption that the $A^2\Sigma$ and $X^2\Sigma$ states follow the Morse potential curve. Recently Sharma constructed accurate potential energy curves for both these states, using the spectroscopic data [9] and calculated Franck-Condon factors [10] which should be regarded as more accurate, although for the principal bands involved, the differences are small. The same remarks are true concerning the sets of r -centroids calculated by Hebert and Tyte [13], Tawde and Korwar [19], and Sharma [10].

Solar Radiation

All the available data on the relative intensity of integrated sunlight has been assessed. It appears that the data of Johnson [20] may be regarded as most truly representative of the solar flux. Spectra of the light of the integrated solar disc (taken at Fort Churchill in October 1965) were examined and some 35 absorption features in the region 4600 to 5270 Å were identified and measured. For the A₂O bands observed, the head (in the R-branch) is in general 2 to 3 Å below the band origin and the rotational lines of the P branch with $K' = 15$ are in general 6.5 to 7.0 Å above the origin. It was found that no lines with an equivalent width greater than 0.5 Å were located within this wavelength region for any band, and hence errors due to the neglect of the absorption features will be small in comparison with those caused by the uncertainty of the relative transition probabilities.

Calculation of Synthetic Spectra

Vibrational. As part of the present investigation, the relative intensity data and apparent source temperatures of the ac arc, exploding foil, and shock tube spectra of Hebert and Tyte [13,14] were converted into three arrays of relative band transition probabilities. In addition, the Franck-Condon factors of Nicholls [18] and Sharma [10] were used as transition probabilities; thus, no variation of R_e with r was assumed.

These five sets of "relative vibrational transition probabilities" and the solar spectral data of Johnson [20] (after it was plotted and smoothed) were used for the calculation of the synthetic spectra. Temperatures of 400, 600, and 800°K were assumed. The relative intensities of the first two bands of the $\Delta v = \pm 1$ sequences are displayed in Figures 17 and 18. Also plotted are the data of Authier [21] who assumed R_e to be a constant and the solar spectrum given by Canavaggia [22]. He also used the Nicholls Franck-Condon Factors [18].

It is seen that considerable doubt concerning the true temperature of the upper atmosphere is introduced as a result of the uncertainty of the relative transition probabilities. For the $\Delta v = +1$ sequence it is seen that the shock tube data gives results which are in fair agreement with those obtained using Franck-Condon factors only, but even here the difference corresponds to a temperature error of some 200°K. Even the slight difference between the Franck-Condon factors of Sharma and Nicholls are sufficient to introduce a possible error of 40°K. From the slope of the curves it is estimated that a 1 percent error in measuring intensity ratios would lead to a 23°K error in temperature. Obviously relative transition probabilities and the relative intensity of the solar spectrum require detailed investigation.

Rotational. The relative rotational transition probabilities of molecules typified as Hund's Case (b) were given by Mulliken [23]. Since each rotational level of any vibrational level may be populated from the adjacent rotational levels of a number of vibrational levels, the relative populations of the

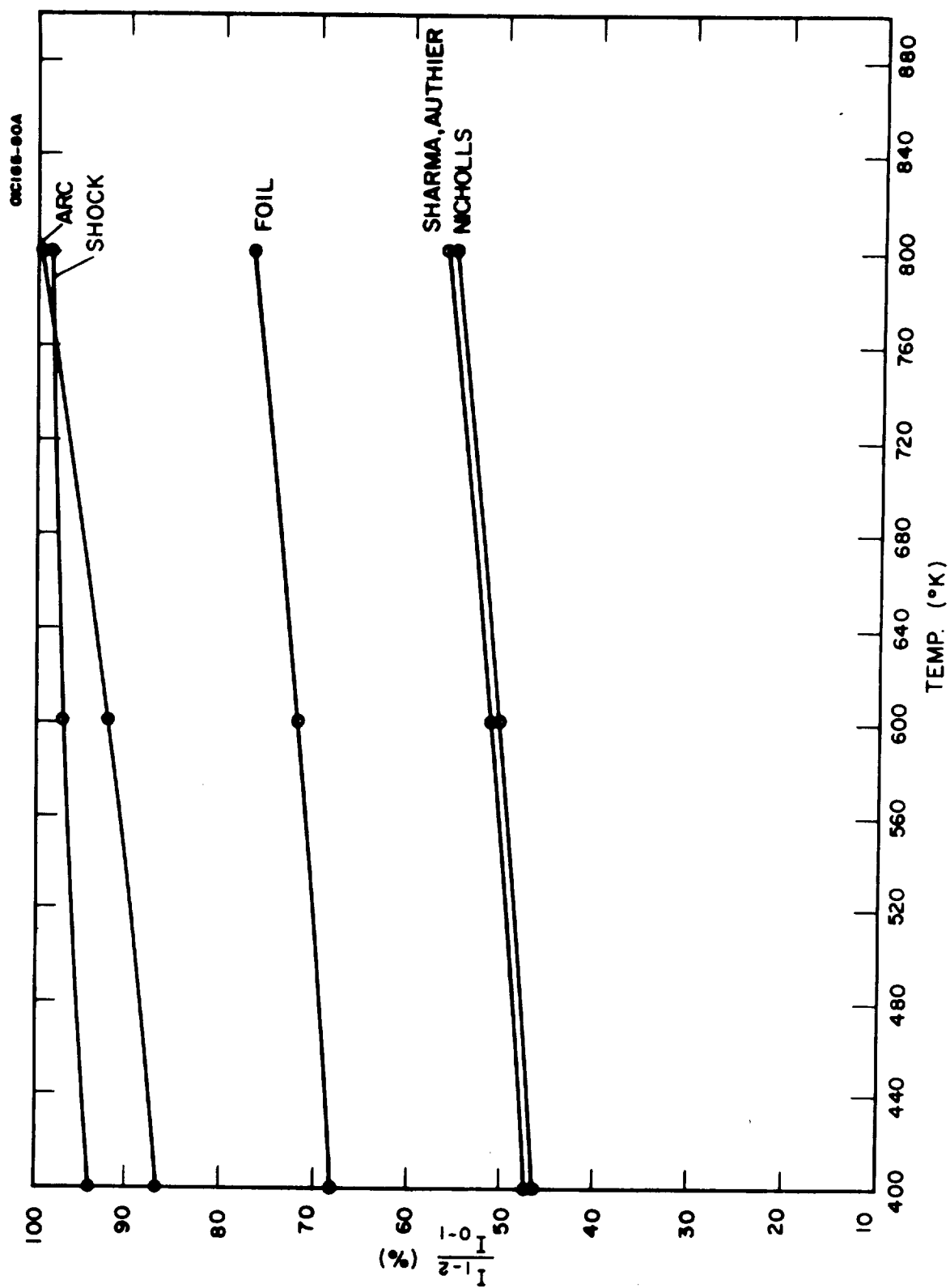


Figure 17. Relative intensity of fluorescence bands in $\Delta v = -1$ as a function of temperature.

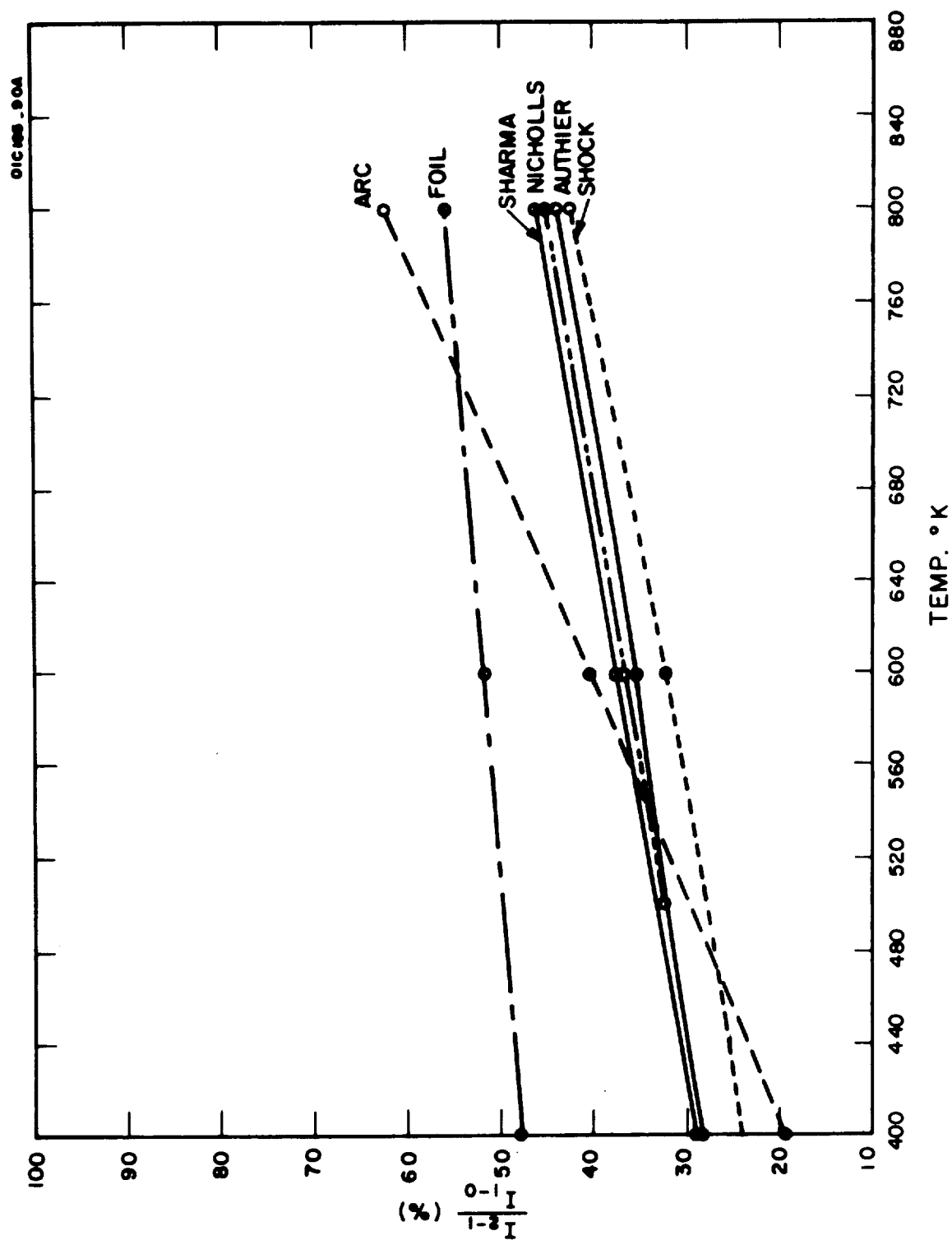


Figure 18. Relative intensity of fluorescence bands in $\Delta v = +1$ sequence as a function of temperature.

rotational levels in any one vibrational level are uncertain to the degree that the relative vibrational transition probabilities are uncertain. In view of this and the fact that synthetic rotational spectra using

$$P_{v',v''} = \text{const} (1 - 0.46 \bar{r}) q_{v',v''} \text{ (Nicholls) [18]}$$

have already been published by Harang [24], it was not thought that a new calculation of synthetic rotational spectra would be justified until better data are available. Moreover, the signal-to-noise ratio of the records obtained at Fort Churchill is not always good enough to show a significant response to two fairly similar synthetic spectra.

Temperatures Obtained at Fort Churchill from the A₁O Trail of 1966

Nike-Apache No. 14.280 was launched at 01.22 GMT 16 September 1966 and ejected 1.75 kg of TMA on the downward leg, covering the altitude range 181 km to 95 km. The time of TMA ejection was +248.4 seconds, and the spectrometer first picked up the A₁O spectrum at +280 seconds and continued to operate until +2710 seconds when the equipment was turned off. Spectra of the top 20 km of the trail could have been obtained for some 15 minutes following turn-off, but the spectrometer had to be modified for the observation of the continuum radiation expected from the next trail(14.281) and the count-down for this was already at T-52 minutes.

During the period of observation the upper part of the trail drifted toward a region of auroral activity (rayed band) and for one or two minutes the two features were visually overlapped (the auroral emission probably took place at lower altitudes, although the possibility of sunlit auroral rays can not be excluded). A spectrum of the aurora alone was also taken for control purposes. The auroral activity increased over the entire sky during the period for which the trail was observed.

Instrumentation. The spectrometer used for these observations was the 0.5 meter "Blue" instrument kindly made available by Mr. W.G. Fastie of the Johns Hopkins University, Baltimore. Although a description of this instrument has been given in the literature [25] the necessary details will be given here:

Focal length	50.0 cm
Grating	10 x 10 cm, 1200 ℓ /mm
Slit circle radius	7.5 cm
Slit length	2.5 cm
Photomultiplier	EMI Type 9558B (S-20 cathode)
Telescope Aperture	12.382 cm
Telescope Focal Length	61.277 cm

If θ is the angle the grating normal makes with the axis the following characteristics apply in the wavelength region of interest:

Wavelength (\AA)	θ	Reciprocal Dispersion ($\text{\AA}/\text{mm}$)
4600	$16^{\circ} 12.3'$	15.14
4916	$17^{\circ} 21.2'$	15.00
5200	$18^{\circ} 23.3'$	14.86

Most spectra were taken with a resolution of 2.4\AA a few were taken at 5.21\AA . The spectrum was recorded on a two-channel chart recorder, moving at 1 cm/sec . The range covered was from 4576.6 to 5284.1\AA giving a scan rate of $12.115\text{\AA}/\text{sec}$. During flyback the two channels were automatically switched to record the high voltage and slit settings. The latter were maintained to give large scale readings on the $\Delta v = \pm 1$ sequences with the $1X$ channel. This resulted in the $0-0$ band overloading this channel, but the outputs could be scaled from the $10X$ channel. One or two spectra were recorded without the $\Delta v = 0$ sequence overloading the $1X$ channel so that accurate values of the relative intensities in the v'' progressions might be determined. These are of interest in order to check the validity of laboratory spectral. Only marked features of the trail were examined so that the temperatures obtained could be given a definite height. These corresponded to altitudes of 165 , 140 , 124 , and 95 km . At 95 km the spectrum also contained a considerable amount of continuum, as might be expected from visual observation.

Temperatures. Most of the spectra were taken at the 165 km level and the analysis of data from this altitude has been carried out in several different ways:

(1) For each scan, relative intensities in the $\Delta v = \pm 1$ sequences were converted directly to temperature. In this way 76 temperature values were obtained, ranging from 558 to 1900°K . This range was divided into 100°K intervals and the frequency of occurrence of a temperature in each interval was noted. Two maxima were obtained, of equal amplitude, in the regions 1001 to 1100°K and 1201 to 1300°K . Dividing the observation into three successive time periods showed this distribution on a smaller scale, so that there is no evidence here for any temperature change with time. Consequently it must be assumed that the heating effect produced by incoming auroral particles has a time constant longer than 35 minutes. On the other hand, when the arithmetic mean of the individual temperatures is calculated for each time period, we obtain values of 1082 , 1131 , and 1213°K , which indicates a steady trend. The average of all 76 readings is 1139°K . It should be noted that this method of analysis weighs data equally, regardless of signal-to-noise quality.

(2) In each sequence the intensity ratios were normalized and added, in order to derive an average intensity ratio before converting to temperature. Again the data are weighed equally. The resulting average intensity ratios are then converted into temperature. The results are given in Table 6.

(3) In this the actual intensities of each band are added numerically for each group of scans. This has the effect of averaging out the noise and weighing each intensity ratio according to its absolute value. The ratio of the relative intensity totals is then converted into temperature. These results are also presented in Table 6.

TABLE 6
TEMPERATURE AT 165 km

Scans	$\Delta v = +1$ Sequence				$\Delta v = 1$ Sequence				Average	
	Unweighted (2)		Weighted (3)		Unweighted (2)		Weighted (3)		All	Principal
	$\frac{I_{2-1}}{I_{1-0}}$	$\frac{I_{3-2}}{I_{1-0}}$	$\frac{I_{2-1}}{I_{1-0}}$	$\frac{I_{3-2}}{I_{1-0}}$	$\frac{I_{1-2}}{I_{0-1}}$	$\frac{I_{2-3}}{I_{0-1}}$	$\frac{I_{1-2}}{I_{0-1}}$	$\frac{I_{2-3}}{I_{0-1}}$		
1-16	866	1139	836	1089	1192	1089	1182	1077	1059	1019
17-28	879	1430	963	1476	1260	1175	1221	1048	1181	1081
29-35	1055	~1800	1035	~1750	1164	1057	1271	1062	1274	1131

It appears that the mean temperature at the 165 km level is about 1130°K during the period of observation, and that over this period a rate of increase in temperature of $7 \pm 2^\circ\text{K}/\text{min}$ was detected. During the entire 35-minute sequence of observations, auroral activity was increasing and ultimately the A₁O glow and auroral rays were superposed. Care was taken to exclude from the above set of observations any which showed signs of contamination by auroral emission features.

The individual temperature determinations made at other altitudes are shown in Figure 19. The numbers beside them indicate the order of occurrence of the scans concerned. The arrows indicate upper limits, in that some of the intensity ratios observed were too low to be converted into a temperature. In this case the average of the other temperatures deduced for this altitude is treated as an upper limit.

Discussion of Results. It is seen that in all cases below 165 km the temperatures obtained are somewhat higher than either of the two standard atmospheres.

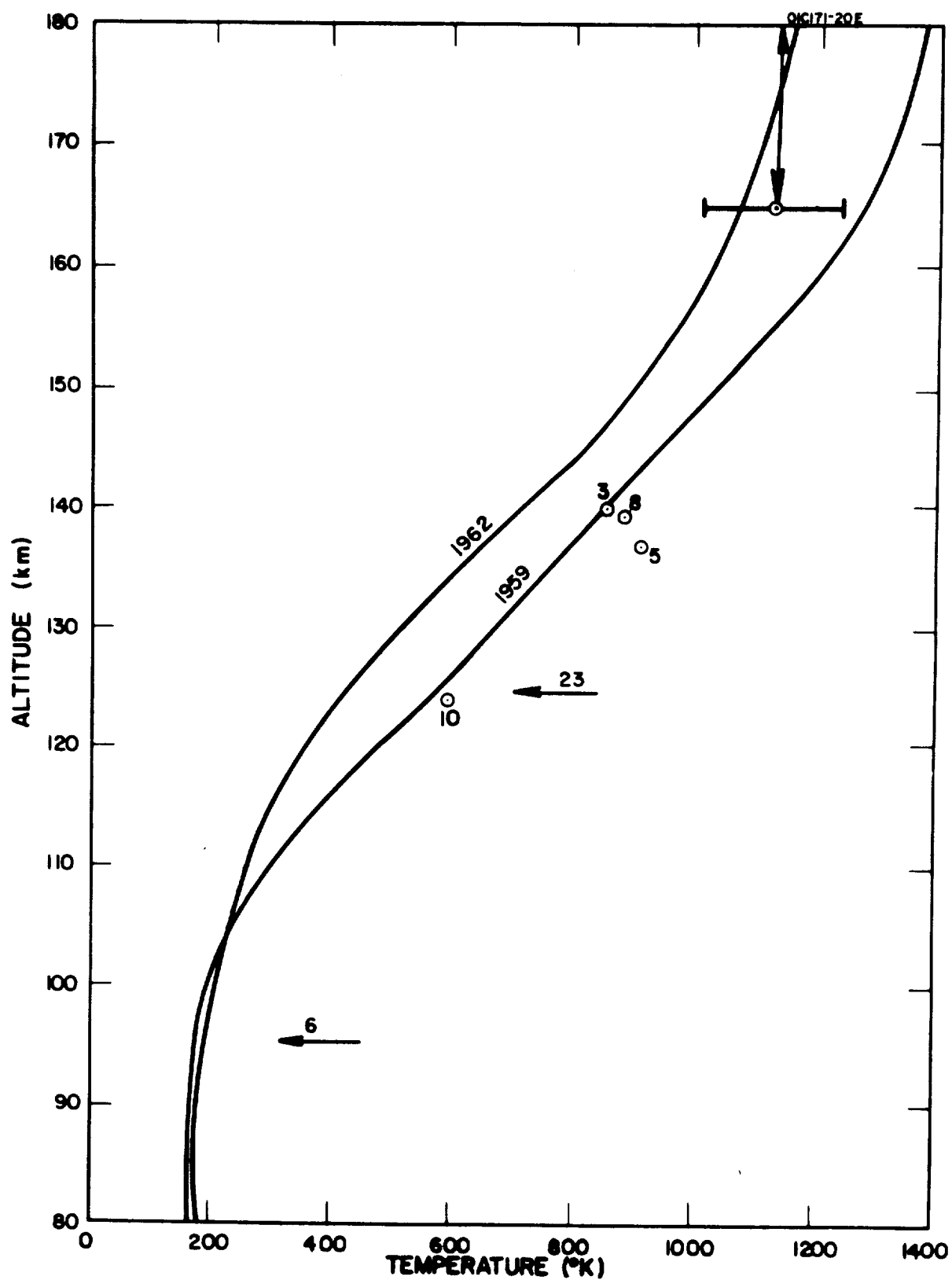


Figure 19. Upper atmosphere temperatures deduced from spectrum of AlO fluorescence at Fort Churchill, October 1966.

However, this is not unexpected, since the conditions were just those required for heating of the upper atmosphere. In the 80 to 100 km region the Kellogg hypothesis [26] is that the poleward migration of atomic oxygen and subsequent recombination can lead to heating of the polar winter mesosphere. It has been shown by Young and Epstein [27] that this process is capable of explaining a temperature rise of $100^{\circ}\text{K}/\text{day}$.

At higher altitudes, the atmosphere is subject to heating by the thin extension of the solar corona which surrounds the earth, as suggested by Chapman [28]. The Earth's magnetic field can shield the upper atmosphere at temperate latitudes from this input, but near the poles the energetic protons can penetrate much closer to the surface of the earth, also causing aurorae. The possibility of heating by incoming auroral particles has already been suggested by Kellogg [26].

Although the lack of certainty concerning the transition probabilities renders the temperatures determined here to have a tolerance of as much as $\pm 150^{\circ}\text{K}$, it is seen that the points obtained do converge to a value of about 200°K at 100 km altitude, as required. Certainly the rate of temperature rise with both time and altitude may be regarded as valid since the most probable intensity ratio versus temperature plots (Figures 17 and 18) have the same slope.

Since the cloud was quite diffuse at the 165 km level, and had a diameter of about 20 km, it is probable that the temperature data obtained from this region corresponds to the altitude range 165 to 180 km, as indicated in Figure 18.

Analysis of the electron temperature data from both flights 14.280 and 14.281 shows that the electron temperature at 170 km is about 1150°K and at 180 km is about 1375°K . Although the data from both these flights was in fair agreement, the first set of data was taken just at the beginning of the buildup of auroral activity, and the second set was taken after some 40 minutes of negligible activity. The auroral activity ceased shortly after the termination of the spectrometer observations.

OBSERVATIONS DURING THE SOLAR ECLIPSE OF 12 NOVEMBER 1966

Introduction

The vapor trail method of observing winds has been limited so far to observations at twilight and night. Daytime observations of sodium trails are feasible with more elaborate observing equipment than is now used (see further comments in the Conclusion and Recommendations). Daytime observations are, however, important both to provide a complete picture of the diurnal variation of neutral wind and to provide observations for investigation of the wind-shear theory for intense daytime sporadic-E layers [29].

A total solar eclipse presents the opportunity of observing winds in the daytime when the observing stations are located in the path of totality. The logistical problems associated with establishing observing sites in remote areas and the improbable but necessary condition requiring clear skies at widespread observing sites has prevented serious consideration of such a program. These difficulties are avoided when the observations are made from a high-flying aircraft as described in a previous section of this report.

The eclipse of 12 November 1966 occurred shortly before local noon on the east coast of southern Brazil. The eclipse path is shown in Figure 20. A Nike-Apache rocket carrying a combined probe/TMA payload was launched at 1402 UT, about eight minutes before totality at the launch site near Cassino, south of Rio Grande. The flight azimuth was selected so that the trail, released during rocket descent, would be as far as possible away from the region of totality.

Vapor Trail Photography

Three camera sites were established in the ground path of totality for the purpose of photographing the TMA trail. In addition, a camera was carried on an aircraft flying in the vicinity. The exposure settings and the film-filter combinations were determined with the expectation that the sky background during totality would approximate a normal twilight background at a solar depression angle of six degrees [30]. Judging from the magnitude and number of stars on the negatives, and from personal observation, the background was somewhat brighter than expected.

The release did occur on schedule starting at 1406 UT as indicated from noise modulation on the telemetry record of the electron probe section of the combined payload. The TMA trail was not visible to the cameras operators in the path of totality, nor is it detected on the photographs taken from these sites. The cloud cover at all three sites was generally 80 percent with cirrus covering most of the field of view and heavy altocumulus in the lower portions. The trail was not observed visually from the aircraft and no attempt was made to photograph it.

SOLAR ECLIPSE : 12 NOVEMBER 1966

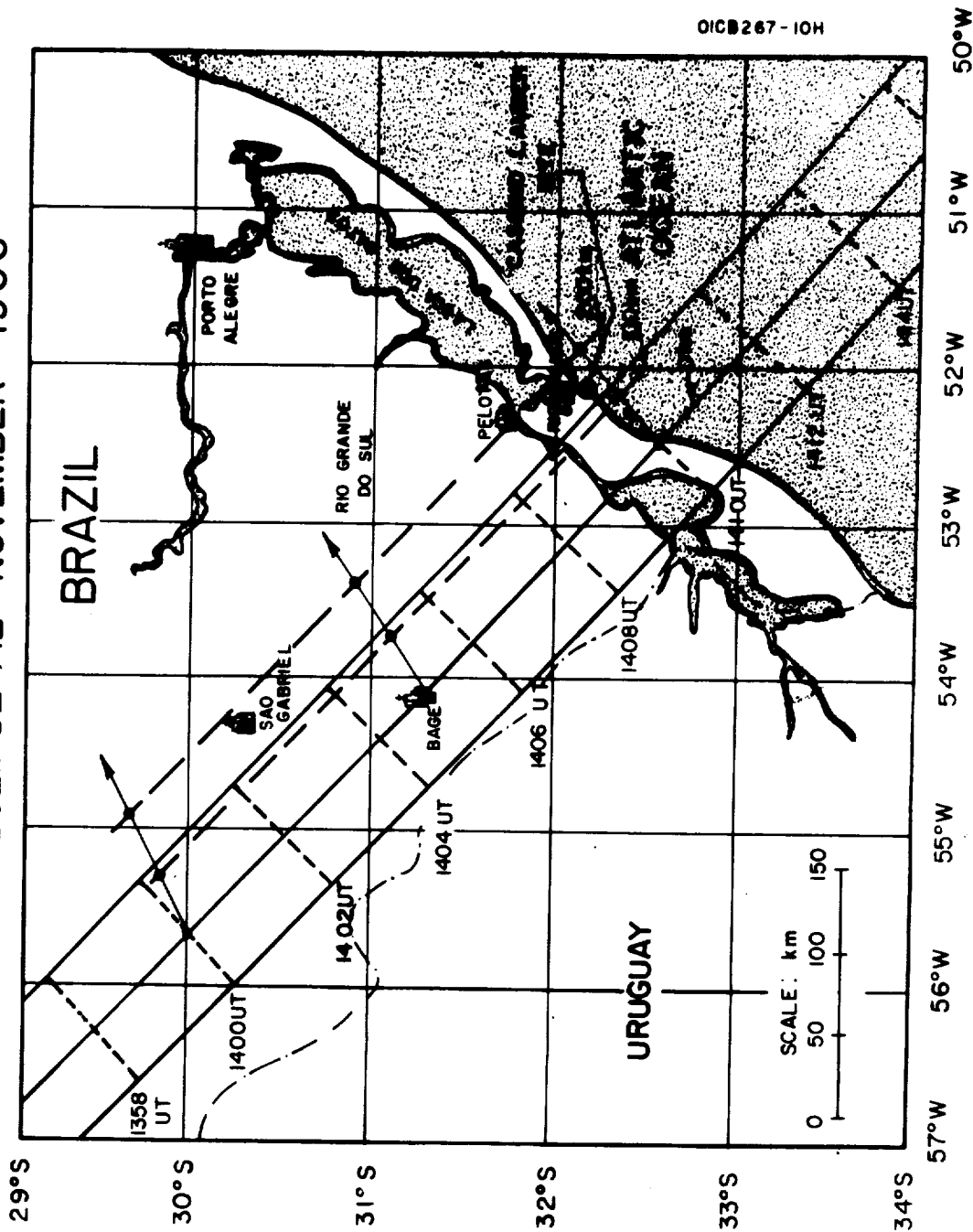


Figure 20. Path of totality at ground level and center line at 0 km and 100 km and 200 km.

The coordinates of the camera sites and their approximate location relative to the launch site were:

<u>SITE</u>	<u>LATITUDE</u>	<u>LONGITUDE</u>	<u>LOCATION FROM LAUNCH</u>
Sarita	32° 37' S	52° 26' W	55 km South
Taim	32° 17' S	52° 34' W	40 km West
Pedro Osorio	31° 53' S	52° 47' W	65 km North West

Each site was equipped with two cameras, a K-24 with a 177-mm lens and a 70-mm camera with a 80-mm lens, both on automatic program at eight frames a minute. The K-24 was set for an aperture of f/16, a three second exposure, and employed 2475 film with a 23A Wratten filter. The 70-mm camera was set at f/16, a one second exposure, and used 2475 film with no filter. The K-24 exposures were very good, but the 70-mm exposures were slightly over-exposed.

The sites at Taim and Sarita were near the center line of ground totality permitting nearly two minutes of photography during totality. The backup site at Pedro Osorio was in totality less than a minute and was hampered by mechanical problems.

Figure 21 is a print of an exposure taken with the K-24 from the Taim site at 1409:30 UT. (At this time the top of the TMA cloud should have been out for over three minutes, and the bottom for approximately one minute). The field of view was 8/10 covered with cirrus with alto cumulous obscuring the bottom third of the field. The TMA trail was not detectable on the negative; the following stars were:

<u>Star</u>	<u>Magnitude</u>
α Sco	1.2
λ Sco	1.7
ϵ Sgr	1.9
θ Sco	2.0
ϵ Sco	2.4
δ Sgr	2.8

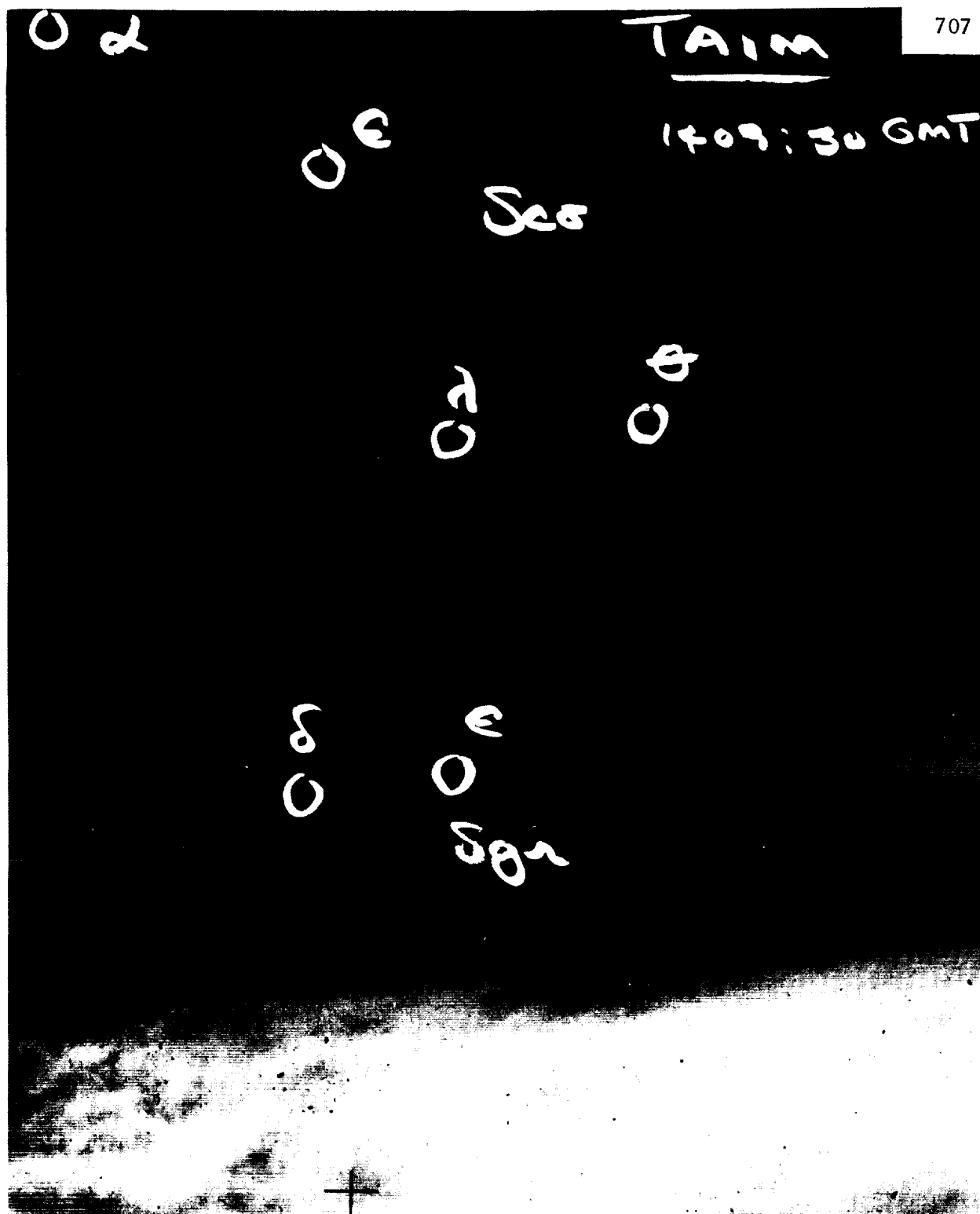


Figure 21.

If the rocket and payload followed the planned trajectory (there is no post-flight trajectory information at this time) on an azimuth of 110°, the pointing angle from Taim would place the center of the field at approximately 115 km and the lower edge at approximately 50 km. Since the TMA would be expected to be most persistent in the range from 95 to 110 km, and the lowest star identifiable on the negative was at an equivalent altitude of approximately 95 km, one would expect the TMA trail to be visible on this negative. One possible explanation of its not being seen is a rocket trajectory that would place the trail in the lower third of the field, or a less likely event, completely out of the field. Alternatively it is possible that the TMA was less bright and persistent than those previously observed, and it could not be detected against the background.

Figure 22 is a print of an exposure from Sarita taken at the same time as that from Taim. Cloud cover in the field is worse than that at Taim with the bottom half obscured by alto-cumulous and heavier cirrus in the top half. At this time, the sun's corona and Venus were visible and the following stars were identified on the negative:

<u>Star</u>	<u>Magnitude</u>
α Sco	1.2
ϵ Sco	2.4
δ Sco	2.5

These were the brightest stars in the field of view; β Sco with a magnitude of 2.9 was not visible on the negative. A magnitude of 2.8 appears to be the lower limit for this film/filter combination with this background.

The pointing angle from Sarita would place the center of the field at approximately 140 km for the planned trajectory. This would have placed the TMA trail almost completely in the lower half of the frame with very little chance of detection behind the alto-cumulous. The cloud conditions here deteriorated during the remainder of totality (approximately 1409:20 to 1411:15 UT) until even the sun's corona and Venus were not visible through the heavy cloud.

Electron Density and Electron Temperature

The profile of electron density obtained from the probe section of the payload is shown in Figure 23. The electron density scale is tentative pending comparison with data from other rockets launched during the eclipse. The profile was obtained shortly before totality with about 5 percent of the sun's disc visible. At this time the electron density had decayed to very small values below about 75 km. The D layer can be identified between 70 and 84 km with the peak occurring at 82 km. The upper side of the layer merges into the lower side of the E layer.

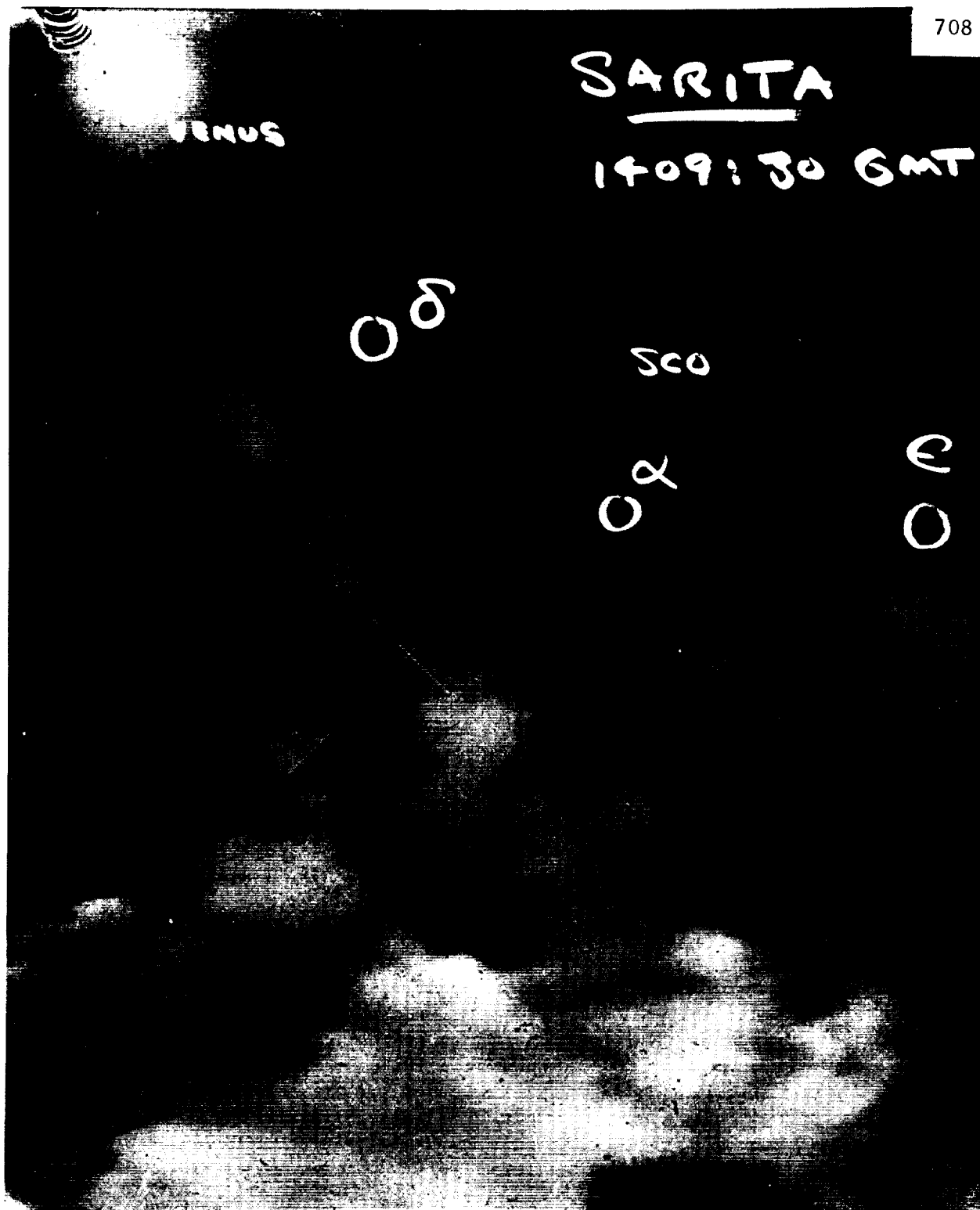


Figure 22.

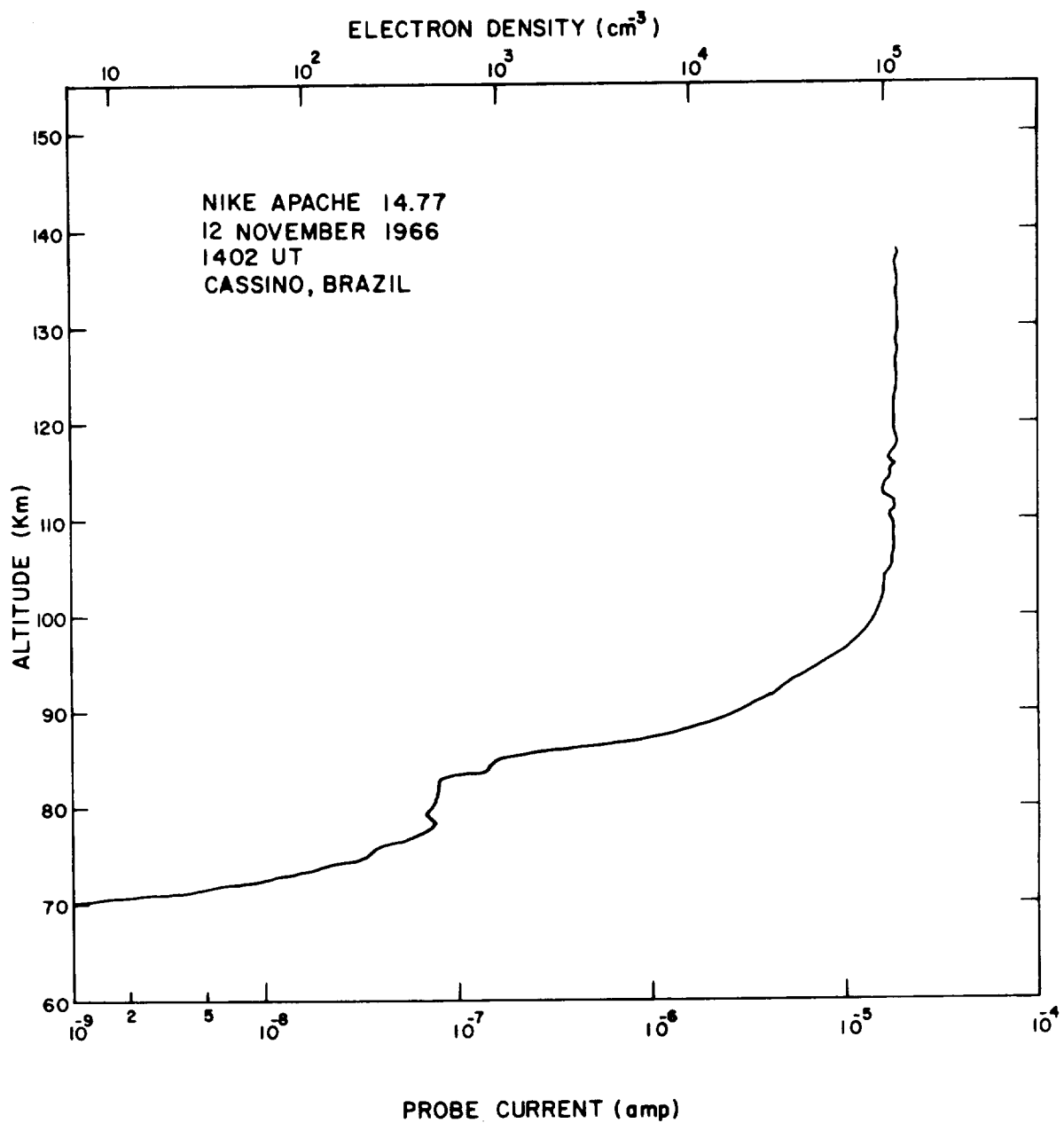


Figure 23. Electron density profile, 12 November 1966, 1402 UT.

The initiation of the TMA release at $T + 240$ sec shows up clearly in its effect both on probe current and on electron temperature. The payload included a modification to the probe not previously used in this program which allows more accurate determination of electron temperature. In this rate of change of current is transmitted on a logarithmic scale. Thus the slope of the log-I-V plot is obtained directly from the telemetry record. In addition to an increase in accuracy, a considerable decrease in effort is required compared with the conventional procedure for analysis of the I-V characteristic. Details of the technique which was developed and used previously on another contract (NASw-1402) will be published elsewhere.

The electron temperature data for this flight is given in Figure 24. Solid points represent individual observations while open circles represent the average of five consecutive readings. The initial readings show very high values of electron temperature. The first data point is at an altitude of 88 km. The temperature rises to a maximum at 93 km then decreases to a minimum value at 103 km. These initial high temperatures are believed to be an instrumental effect. A similar effect has been observed on other flights with no TMA release on the ascent profile but does not reproduce on the descent profile.

Release of the TMA produces an immediate decrease in electron temperature measured by the probe. A periodicity in the variation of electron temperature in the later part of the flight is attributable to a "beat" between the 2-second interval between temperature observations (which each take about 0.1 second) and the spin of the vehicle (6 rps, nominal). The TMA release produces a modulation of probe current (at +2.7 volt) at the spin rate (which is itself observed on the aspect magnetometer). Defining the phase angle of the vehicle in its rotation by taking zero degree to correspond with maximum probe current it is found, as shown in the subsidiary plot, that the maximum electron temperatures occur at a nearly constant phase angle relative to the variation in probe current. Similarly the minimum are about 180 degrees out of phase with the maxima. It is interesting to note that the electron temperatures observed during the TMA release are reduced below ambient values.

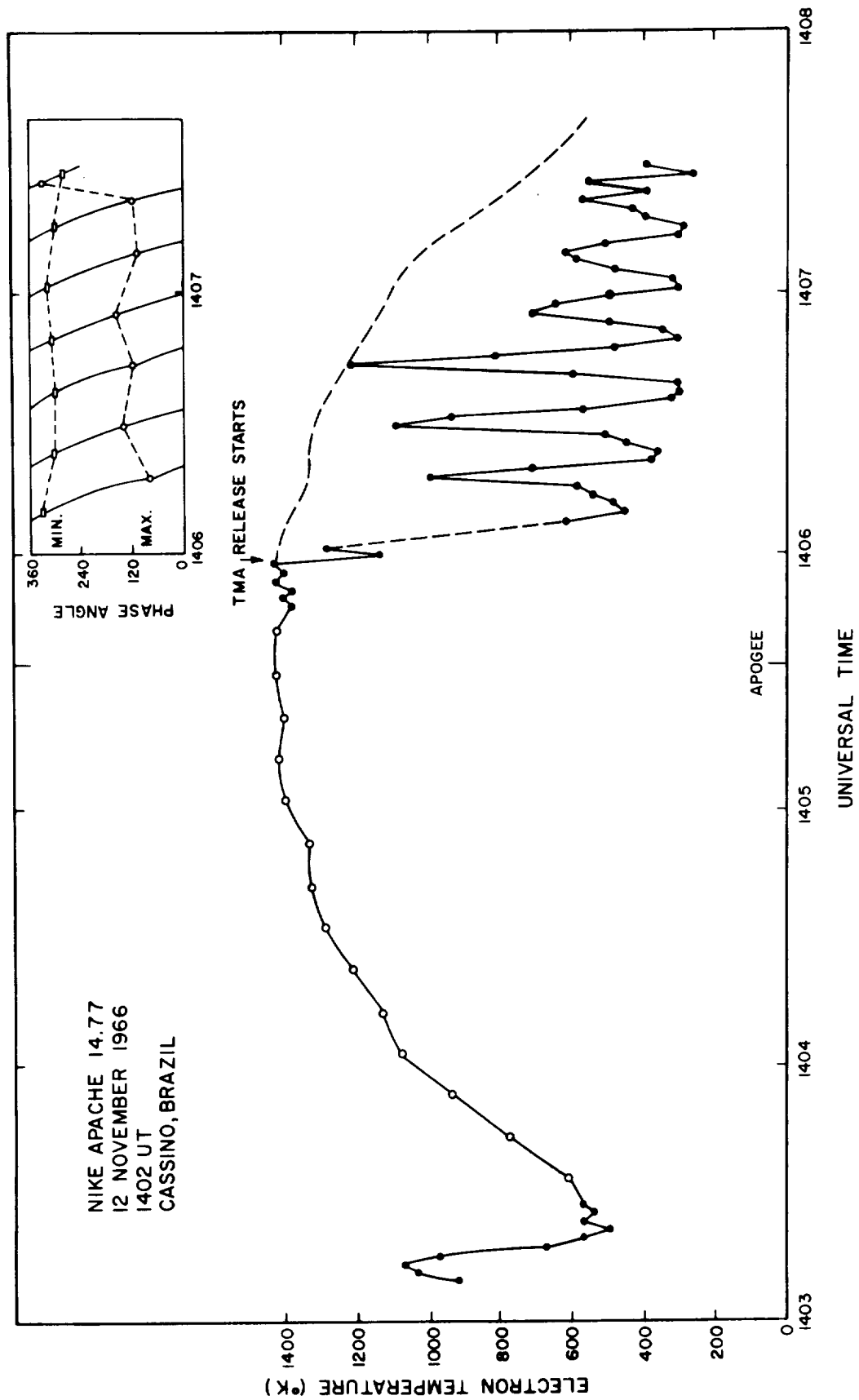


Figure 24. Electron temperature observations showing effect of TMA release.

CONCLUSIONS AND RECOMMENDATIONS

Electron Density and Wind Profiles

The simple wind-shear theory gives the following relation between the vertical component of ion drift velocity V_z and the horizontal components of the neutral winds V_x and V_y

$$V_z = \frac{\rho_+}{1 + \rho_+^2} V_x \cos \phi - \frac{1}{1 + \rho_+^2} V_y \sin \phi \cos \phi$$

where ϕ is the dip angle and ρ_+ is the ratio of the ion-neutral collision frequency to the ion gyro-frequency. The parameter ρ_+ , which is a function of altitude, determines the relative importance of the eastward wind component V_x and the northward wind component V_y . In the height range in which sporadic-E^x layers are found, i.e., up to about 120 km, the eastward component dominates and the altitude at which the layer forms is at the point of zero velocity in an east-west wind shear. North-south wind shears are important at higher altitudes. One weakness of the simple theory is that sporadic-E layers are not found at altitudes much above 120 km although adequate wind shears exist there.

The role of the dip angle ϕ is also interesting. In the important region below 120 km, where the east-west wind component dominates, the vertical ion drift is proportional to $\cos \phi$. This term implies that the effectiveness of a given wind shear increases as the dip angle decreases. This is consistent with the observation of the increased frequency of occurrence of thin-layer (blanketing) sporadic E at temperate latitudes compared with high latitudes, a fact which gave great impetus to the original acceptance of the wind-shear theory.*

The two factors $\cos \phi$ and $\cos \phi \sin \phi$ are shown as functions of the geomagnetic latitude in Figure 25. It will be noted that $\cos \phi$ shows a roughly linear change with latitude and that $\cos \phi \sin \phi$ has a maximum value of 0.5 at a latitude of 26.5 degrees (dip angle 45 degrees). The geomagnetic latitudes of the launch sites at Wallops Island and Fort Churchill are indicated. The values of the two factors $\cos \phi$ and $\cos \phi \sin \phi$ at the latitude of Fort Churchill are almost exactly half those at the latitude of Wallops Island. Thus the vertical drift velocity of the ionization would, over Fort Churchill, be half that over Wallops Island for the same wind structure. On the basis

*An anomalous situation exists near the geomagnetic equator in which, contrary to the formulation given above, the incidence of thin-layer sporadic E decreases sharply within a few degrees of magnetic latitude. Axford and Cunlold [31] have recently shown that this can be explained in terms of the wind-shear mechanism.

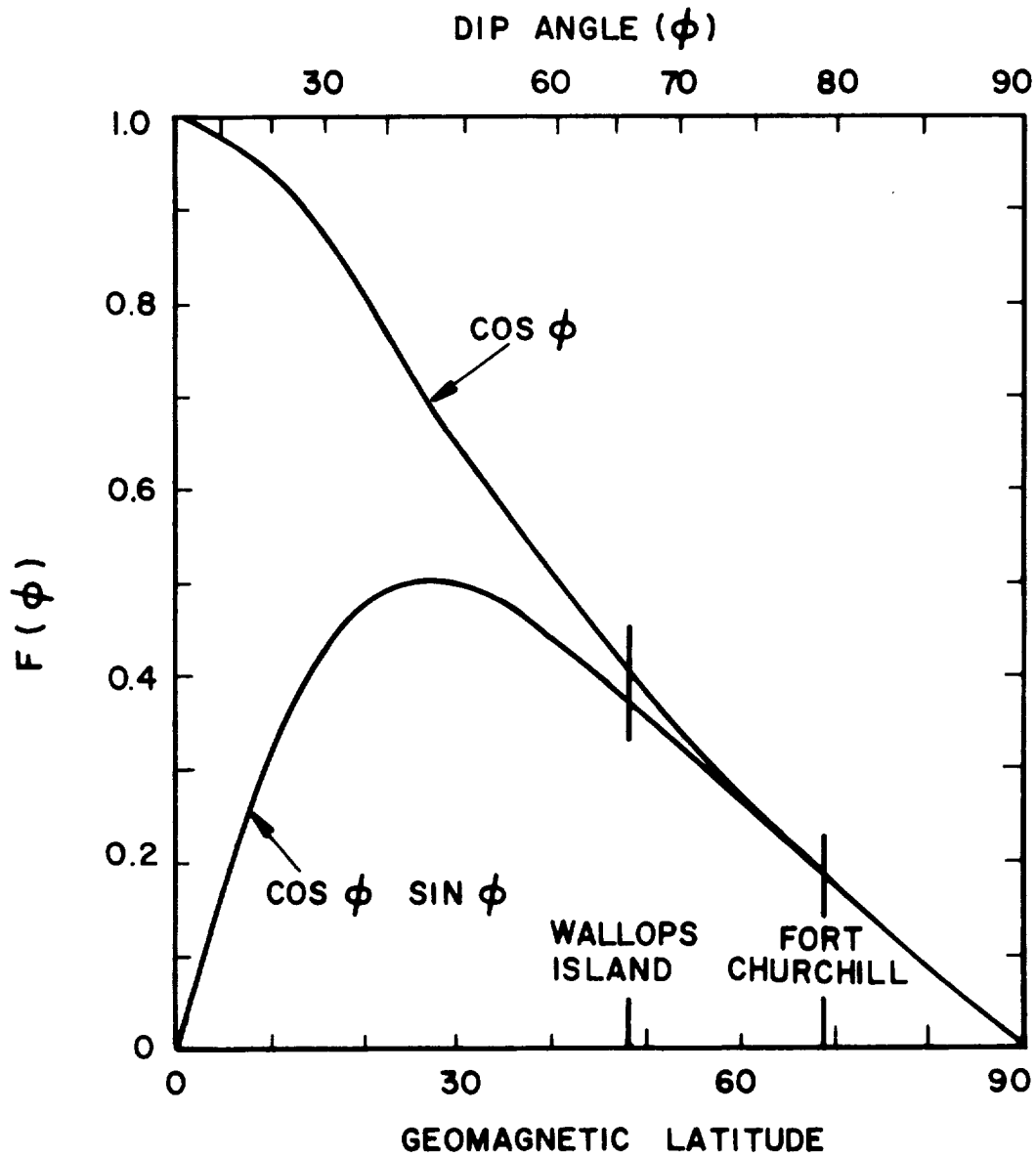


Figure 25. The functions $\cos \phi$ and $\cos \phi \sin \phi$ vs geomagnetic latitude.

of the available rocket data, thin-layer sporadic E is never observed at Fort Churchill whereas it has been seen on frequent occasions at Wallops Island. One possible explanation is that the wind structure at Fort Churchill is systematically different from that at Wallops Island. The large quantity of available data tends to refute this possibility. This point cannot be resolved at present and provides another illustration of the weakness of the wind-shear theory.

An aspect of the wind-shear theory which requires further investigation is the time-variation that occurs both in the wind structure and electron density profiles. The time scale for changes in these profiles is of the order of an hour, i.e. significant changes in wind structure are seen only when time intervals greater than one hour are considered. Similarly the persistence of a sporadic E layer is of the order of an hour.

It is recommended that the time-variation of both wind and electron density profiles be observed in closely-spaced series of rocket firings with the objective of testing the validity of a redistribution type of process for formation of sporadic E layers. It is intended to treat the problem generally by making no assumptions about the actual mechanism which results in the vertical transport of ionization but rather to reverse the usual procedure and, from the time-variation of the electron density profile, obtain the vertical component of ionization drift as a function of height. This can then be compared with the simultaneously observed wind profiles to establish a relation between actual wind (horizontal) velocities and the vertical velocity of the ionization.

The vertical transport of ionization can be derived from the electron density profiles in the manner outlined as follows: Equation A-1 (Appendix A) is re-written, neglecting horizontal variations*

$$\frac{\partial N}{\partial t} = - \frac{\partial}{\partial z} (wn) + q - \alpha N^2 - \beta N + \frac{\partial}{\partial z} (D \frac{\partial N}{\partial z})$$

Integrating between the limits z_0 and z , we have, after some rearrangement:

$$\begin{aligned} w(z,t) N(z,t) &= w(z_0,t) N(z_0,t) + D(z) \frac{\partial N(z,t)}{\partial z} \\ &\quad - D(z_0) \frac{\partial N(z_0,t)}{\partial z_0} - \int_{z_0}^z dz' \frac{\partial N(z',t)}{\partial t} \\ &\quad + \int_{z_0}^z dz' [q(z') - \beta(z')N(z',t) - \alpha(z') N(z',t)^2] \end{aligned}$$

* See Table A.1, (page 70), for definitions of symbols.

The electron density, $N(z,t)$ is measured directly. Its vertical derivative, $\partial N/\partial z$, can be calculated from the measurements. If a short time separates consecutive measurements of N , then

$$\frac{\partial N}{\partial t} \approx \frac{\Delta N}{\Delta t}, \quad \Delta N \equiv N(t + \Delta t) - N(t)$$

Accordingly, the term containing the time derivative of N can be calculated. Of the other quantities the diffusion coefficient D , the recombination coefficient α , and the attachment coefficient β may be regarded as known. The production rate q may be set equal to zero (at night), or treated as a variable parameter. The only unknown quantity on the right side is $w(z_0)$, the ionization drift velocity at the reference level z_0 . The term

$$w(z_0) N(z_0)$$

can be neglected by a special choice of z_0 . If z_0 is chosen sufficiently low, then $N(z_0)$ will have a negligible value. Or z_0 may be chosen to coincide with a minimum of N (if such a level clearly exists), or a maximum of N . At such points the drift velocity $w(z_0)$ vanishes for many examples of the redistribution theory. The equation then is sufficient for the calculation of $w(z,t)$.

This velocity $w(z,t)$ can then be compared with the instantaneous value predicted by the wind-shear theory equation. It will immediately be evident whether, within the accuracy allowed by the experimental observations, the data support this particular wind-shear theory. If agreement is not good but an empirical relation can be found between the vertical velocity of ionization drift and the horizontal components of neutral wind, then a redistribution mechanism is supported and an attempt made to derive a theory which explains the experimentally determined relationship.

These observations would require a series of rocket flights during a single night, each rocket carrying an electron density probe and a vapor canister. These would be launched sequentially at intervals not exceeding one hour. A program of this nature at a mid-latitude site such as Wallops Island would be a logical extension of the investigation of sporadic-E layer formation.

Another experiment which is now technically feasible is the investigation of daytime sporadic-E layers, initially at mid-latitudes. The electron density profiles of these day-time layers have been observed on many occasions but as yet no day-time wind profiles are available. Since, as has been pointed out earlier, the higher electron densities of the day-time E region compared with those at night provide a more severe test of the wind-shear theory (or, for that matter, any redistribution theory), it is now urgently required that wind profiles be obtained during the occurrence of day-time sporadic E.

Several methods of day-time wind observation using the vapor trail method have been considered. It appears possible that the required discrimination against background illumination can be obtained with optical filtering in the case of a sodium release. This is considered a most important development for the further investigation of the relation between winds and electron density.

Aircraft Observations of the Wind Structure

The value of a high-flying aircraft as a platform for photography in the vapor trail method of wind determination was successfully demonstrated during the series of rocket launches at Fort Churchill. Comparison of the wind hodograph deduced from the aircraft photographs with that obtained from the ground stations shows generally good agreement. The method requires an accurate knowledge of the position of the aircraft while the photographs are being taken. This is obtained by radar tracking of the aircraft which proved, at Fort Churchill, to be a major problem. This can no doubt be avoided in future use of the aircraft.

The particular values of the aircraft as an observing platform are (1) the wind determination becomes much less dependent on weather than when ground stations are used, and (2) the vapor trail technique can be used at locations where no suitable sites are available for cameras.

REFERENCES

1. Whitehead, J D., "The Formation of the Sporadic-E Layer in the Temperate Zones," J. Atmos. Terr. Phys., 20, 49-58 (1961).
2. MacLeod, M.A., "Sporadic E Theory. I. Collision-Geomagnetic Equilibrium," J. Atmos. Sci., 23, 96-109 (1966).
3. Wright, J.W., C.H. Murphy and G.V. Bull, "Sporadic E. and the Wind Structure of the E Region," J. Geophys. Res. 72, 1443-1460 (1967).
4. Bedinger, J.F. and H.B. Knafllich, "Observed Characteristics of Ionospheric Winds," Rad. Sci., 1, 156-168 (1966).
5. Layzer, D., "Gravity Shock Waves and Stratification in the Upper Atmosphere," Nature 213, 576-578 (1967).
6. Whithead, J.D., "Sporadic E in Middle Latitudes," Nature 214, 261 (1967)
7. Smith, L.G., J.F. Bedinger, and G.T. Best, "Measurement of Upper Atmospheric Ionization and Winds with a Combined Payload," Interim Report, Contract No. NASw-1083, GCA Tech Rpt No. 66-11-N (1966).
8. Tyte, D.C. and R.W. Nicholls, "Identification Atlas of Molecular Spectra I. The AlO $A^2\Sigma-X^2\Sigma$ Blue-Green System," London, Ontario (1964).
9. Sharma, A., "The True Potential Energy Curves of $X^2\Sigma$ and $A^2\Sigma$ states of the AlO Molecule," J. Quant. Spectros. Radiat. Transfer. 7 282 (1967).
10. Sharma, A., "The Franck-Condon Factor and r-Centroids of $A^2\Sigma-X^2\Sigma$ Band System of AlO ," J. Quant. Spectros. Radiat. Transfer. 7, 289 (1967).
11. Nicholls, R.W. and W.R. Jarman, "r-Centroids: Average Internuclear Separations Associated with Molecular Bands," Proc. Phys. Soc. 69A, 253 (1956).
12. Nicholls, R.W., "Studies upon Transition Probabilities and Molecular Excitation," Ann. de Geophys., 14, 208 (1958).
13. Hebert, G.R. and D.C. Tyte, "Intensity Measurements on the $A^2\Sigma-X^2\Sigma$ System of Aluminum Oxide," Proc. Phys. Soc. 83, 629 (1965).
14. Tyte, D.C. and G.R. Hebert, "The Electronic Transition Moment of the $A^2\Sigma-X^2\Sigma$ System of AlO ," Proc. Phys. Soc. 84, 830 (1964).
15. Tawde, N.R. and V.M. Korwar, "Electronic Transition Moment Variation in Bands of AlO ($A^2\Sigma^+-X^2\Sigma^3$) System," Proc. Nat., Inst. Science India 29A, 325 (1963).

REFERENCES (continued)

16. Tawde, N.R. and V.M. Korwar, "Effective Vibrational Temperature as a Variant of Electronic Transition Moment in AlO ($A^2\Sigma^+-X^2\Sigma^+$) System," Indian J1, Pure and Applied Physics 3, 198 (1965).
17. Tyte, D.C., "The Effect of Environmental Conditions on Band Strength," Quant. J. Spectrosc. Radiat. Transfer 5, 545 (1965).
18. Nicholls, R.W., "Franck Condon Factors to High Vibrational Quantum Numbers: II: SiO MgO , SvO , AlO VO , NO ," J. Res. Nat. Bur. Stds., 66A, 227 (1962).
19. Tawde, N.R. and Korwar, V.M., "Franck Condon Factors and r-Centroids for the Aluminum Monoxide $A^2\Sigma^+ + X^2\Sigma$ Band System," Proc. Phys. Soc. 80, 794 (1962).
20. Johnson, F.S., "The Solar Constant," Jour. of Meteorology 11, 431 (1956).
21. Authier, B., "Mesures de temperature de l'ionosphere and partir de la fluorescence de molecules prodistes artificiellement au moyen de fusees," Ann. de Geophys. 20, 353 (1964).
22. Canavaggia, R., D. Chalonge, M. Egger-Moreau, H. Oziol-Peltey "Recherches sur le Spectre Continu du Soleil III: Spectre continu de centre du Disque Entre 3200 et 5000 \AA ," Ann. d'Astrophys. 13, 355 (1950).
23. Mulliken, R.A., "The Interpretation of Band Part IIC, Empirical Band Types," Rev. Mod. Phys., 3, 89 (1931).
24. Harang, O., " AlO Resonant Spectrum for Upper Atmosphere Temperature Determination," AFCRL Environmental Research Papers No. 192, AFCRL No. 66-314 (1966).
25. Fastie, W.G., "Instrumentation for Far-Ultraviolet Rocket Spectrophotometry," J. Quant. Spectros. Radiat. Transfer 3, 507 (1963).
26. Kellogg, W.W., "Chemical Heating above the Polar Winter Mesopause in Winter," J. Meteorology 18, 373 (1961).
27. Young, C., and E. Epstein, "Atomic Ozygen in the Polar Winter Mesosphere," Jour. Atmos. Sci. 19, 435 (1962).
28. Chapman, S , "The Thermosphere - The Earth's Outermost Atmosphere," Chapter I of "Physics of the Upper Atmosphere," (ed. J.A. Ratcliffe) New York (1960).
29. Bedinger, J.F. and L.G. Smith, "Measured Wind Shears and Electron Densities," Space Research VII, North-Holland Pub. Co., Amsterdam (1966).

REFERENCES (continued)

30. Sharp, W.E., J.W.F. Lloyd, and S.M. Silverman, "Zenith Skylight Intensity and Color during the Total Solar Eclipse of 20 July 1963," Appl. Opt. 5, No. 5, 787 (1966).
31. Axford, W.I. and D.M. Cunnold, "The Wind-Shear Theory of Temperate Zone Sporadic E," Rad. Sci. 1, 191-198 (1966).

APPENDIX A

TIME-DEPENDENT REDISTRIBUTION THEORY

The variation of electron density in the ionosphere is governed by the equation expressing the local conservation of charge:

$$\frac{\partial N}{\partial t} = - \nabla \cdot (\underline{v} N) + q - L + \nabla \cdot (D \nabla N) \quad (A-1)$$

where N is the electron density, \underline{v} the drift velocity, q and L the production and loss rates respectively, and D the coefficient of diffusion.* The quantity $\underline{v} N$ is referred to as the "induced flux," while $D \nabla N$ represents the diffusive flux. Equation (A-1) states that the rate of change of the electron density is diminished by the net outward flux due to drift and diffusion, increased by the local rate of electron production, and decreased by the local rate of electron loss.

The occurrence of horizontal layers of enhanced ionization in the E region (sporadic-E layers) must ultimately result from the variation with height of one or more of the quantities \underline{v} , q and L . Any theory that attributes the formation of sporadic E primarily to the vertical variation of \underline{v} may be reasonably called a "redistribution theory." The "wind shear" theory may be described as a "steady state" redistribution theory and $\partial N / \partial t$ is set equal to zero in Equation (A-1). This section considers a redistribution theory, based on a simplified version of Equation (A-1), that puts emphasis on the location and initial development of the layers of enhanced ionization.

The following assumptions are considered reasonable for middle latitudes:

- (1) Since the horizontal extent of E_s layers is of the order of hundreds of kilometers, the horizontal variation of all quantities may be neglected.
- (2) A single species of positive ions is present, whence the recombination term has the form αN^2 , where α is the recombination coefficient. The loss term is then given by

$$L = \alpha N^2$$

(The electron attachment term, βN , where β is the effective reaction rate for electron attachment, will be considered negligible here.) (3) The night-time value of the production rate is negligible:

$$q \approx 0$$

*A complete list of symbols for this section is given in Table A-1.

TABLE A-1
LIST OF SYMBOLS

V	Horizontal component of neutral wind velocity
Z	Altitude
N	Electron density
t	Time
\underline{v}	Ionization drift velocity
q	Rate of production of electrons
L	Rate of loss of electrons
D	Diffusion coefficient
α	Recombination coefficient
β	Attachment loss coefficient
w	Vertical component of ionization drift velocity
M	Reciprocal electron density ($=N^{-1}$)
ξ	Characteristic coordinate, defined by Equation (A-4)
ζ	Defined in Equations (A-6) and (A-7)
γ	Defined in Equation (A-12)
ω	Defined in Equation (A-26)
ω_1	Ion gyro-frequency
ν_1	Ion collision frequency
X	Geomagnetic dip angle
V_x, V_y	Components of neutral wind velocity toward geomagnetic east and north
w_p	Ionization drift velocity associated with polarization field

(4) The diffusion term is unimportant, except for very narrow layers. (5) The drift velocity has a vertical component only, and this component, w , is a known, time-independent function of height.

Assumption (4) breaks down at a certain stage of the development of a layer. Similarly, suitable time limits determine the validity of assumptions (1) and (5). Assumption (2) is probably valid above a certain height most of the time, and over most of the E region at night.

These simplifying assumptions reduce Equation (A-1) to the form

$$\frac{\partial N}{\partial t} = - \frac{\partial}{\partial z} (wN) - \alpha N^2 \quad (\text{A-2})$$

The general solution of this equation may be written in terms of the quantity M , defined as the reciprocal of the electron density:

$$M = N^{-1} \quad (\text{A-3})$$

and in terms of a characteristic coordinate ξ defined by the differential relation

$$d\xi = dz/w(z) \quad (\text{A-4})$$

Thus

$$M(z,t) = \frac{w(z)}{w(\xi)} M(\xi,0) + \alpha w(z) \int_{\xi}^z \frac{dz'}{[w(z')]^2} \quad (\text{A-5})$$

where ξ is defined as follows: If Equation (A-4) is solved so that z is obtained as a function of ξ ,

$$z = f(\xi) \quad (\text{A-6})$$

then

$$\xi = f(\xi - t) \quad (\text{A-7})$$

Finally, $M(z,0)$ is the initial value of $M(z,t)$. It must be emphasized that Equation (A-5) is a formal solution only; the definition of ξ may encounter difficulties owing to the singularities of Equation (A-4). The following examples are chosen to demonstrate a number of interesting conclusions.

Model 1:

$$w = w_o + w_1 z \quad (A-8)$$

This may be called the "Uniform Wind Shear" model. The solution is

$$M(z,t) = \exp(w_1 t) M(\zeta, 0) + \frac{\alpha}{w_1} [\exp(w_1 t) - 1] \quad (A-9)$$

where

$$\zeta = \exp(-w_1 t) z - \frac{w_o}{w_1} [1 - \exp(-w_1 t)] \quad (A-10)$$

Note that if the initial density is independent of height, it remains such for all time. Thus even a strong wind shear (of the "correct" sign) will not necessarily lead to the formation of a layer of enhanced ionization.

Model 2:

$$w = w_o + w_1 z + w_2 z^2, \quad w_1^2 > 4 w_o w_2 \quad (A-11)$$

In this model the vertical drift velocity varies quadratically with height and vanishes at the heights

$$z_{\pm} = -\frac{w_1 \pm \gamma}{2w_2}, \quad \gamma = + (w_1^2 - 4 w_o w_2)^{\frac{1}{2}} \quad (A-12)$$

In terms of z_+ and z_- w may be written as

$$w = w_2 (z - z_+) (z - z_-) \quad (A-13)$$

Note that

$$\left. \frac{\partial w}{\partial z} \right|_{z=z_{\pm}} = \mp \gamma \quad (A-14)$$

The general solution for this model is

$$\begin{aligned}
M(z,t) = & \gamma^{-2} \cosh^2 (\gamma t/2) [\gamma + (w_1 + 2w_2 z) \tanh (\gamma t/2)]^2 M(\xi, 0) \\
& + \alpha \gamma^{-2} \{w_2^2/\gamma [(z-z_+)^2 e^{\gamma t} - (z-z_-)^2 e^{-\gamma t}] - 2w_2^2 t(z-z_+)(z-z_-) \\
& - (w_1 + 2w_2 z)\} \quad (A-15)
\end{aligned}$$

where

$$\xi = \frac{\gamma z - (2w_0 + w_1 z) \tanh (\gamma t/2)}{\gamma + (w_1 + 2w_2 z) \tanh (\gamma t/2)} \quad (A-16)$$

Equivalently,

$$\begin{aligned}
M(z,t) = & \frac{w_2^2}{\gamma^2} [e^{\gamma t/2} (z-z_+) - e^{-\gamma t/2} (z-z_-)]^2 M(\xi, 0) \\
& + \frac{w_2^2}{\gamma^2} \frac{\alpha}{\gamma} \left[(z-z_+)^2 e^{\gamma t} - (z-z_-)^2 e^{-\gamma t} - 2t(z-z_+)(z-z_-)\gamma - \frac{\gamma(w_1 + 2w_2 z)}{w_2^2} \right] \quad (A-17)
\end{aligned}$$

Asymptotically, that is for $\gamma t \gg 1$:

$$\xi \rightarrow z_- \quad (A-18)$$

$$M(z,t) \rightarrow \frac{w_2^2}{\gamma^2} [\alpha/\gamma + M(z_-, 0)] (z-z_+)^2 e^{\gamma t} \quad (A-19)$$

except in the vicinity of $z = z_+$, where

$$M(z,t) \rightarrow \alpha/\gamma \quad (A-20)$$

M attains its minimum value at $z = z_+$. Hence this is the point of highest electron density. This maximum in the electron density occurs irrespective of the initial conditions. The width of the peak at half-maximum is given approximately by

$$2|z_{1/2} - z_+| = 2 \frac{\gamma}{w_2} e^{-\gamma t/2} [1 + \gamma/\alpha M(z_-, 0)]^{-1/2} \quad (\text{A-21})$$

In the vicinity of the maximum ($z = z_+$), the ratio of the diffusion term to the recombination term is

$$\frac{D}{\alpha} \frac{\partial^2 M}{\partial z^2} \rightarrow \frac{2D}{\alpha} \frac{w_2^2}{\gamma^2} [\alpha/\gamma + M(z_-, 0)] e^{\gamma t} \quad (\text{A-22})$$

The diffusion term will be negligible provided

$$e^{\gamma t} < \frac{1}{2D} \frac{\gamma^3}{w_2^2} \left[1 + \frac{N_{\max}}{N(z_-, 0)} \right]^{-1/2} \quad (\text{A-23})$$

To obtain a numerical estimate, we use the following values:

$$\gamma = 2 \times 10^{-3} \text{ s}^{-1}, \quad w_2 = 10^{-6} \text{ s}^{-1} \text{ m}^{-1}, \quad D \leq 5 \times 10^2 \text{ m}^2 \text{ s}^{-1},$$

and

$$\frac{N_{\max}}{N(z_-, 0)} = 8.$$

Then

$$e^{\gamma t} < \frac{8}{3} \quad (\text{A-24})$$

Thus diffusion effects maybe neglected until γt is approximately unity.

Model 3:

$$w = w_0 + w_1 z + w_2 z^2, \quad w_1^2 < 4 w_0 w_2 \quad (\text{A-25})$$

The vertical drift velocity varies quadratically with height, but it does not vanish anywhere. If w is written in the form

$$w = w_2 \left[\left(z + \frac{w_1}{2w_2} \right)^2 + \frac{\omega^2}{4w_2^2} \right], \omega = + (4w_0 w_2 - w_1^2)^{1/2} \quad (\text{A-26})$$

then the absolute value of w attains its minimum value at $z = -w_1/2w_2$. The general solution is:

$$\begin{aligned} M(z, t) &= \omega^{-2} [w \cos(\omega t/2) + (w_1 + 2w_2 z) \sin(\omega t/2)]^2 M(\xi, 0) \\ &+ \alpha \omega^{-2} \left\{ 2w_2^2 t \left[\frac{\omega^2}{4w_2^2} + \left(z + \frac{w_1}{2w_2} \right)^2 \right] + (w_1 + 2w_2 z) (1 - \cos \omega t) \right. \\ &\left. + \frac{2w_2^2}{\omega} \left[\frac{\omega^2}{4w_2^2} - \left(z + \frac{w_1}{2w_2} \right)^2 \right] \sin \omega t \right\} \end{aligned} \quad (\text{A-27})$$

where

$$\xi(t) = \frac{\omega z - (2w_0 + w_1 z) \tan(\omega t/2)}{\omega + (w_1 + 2w_2 z) \tan(\omega t/2)} \quad (\text{A-28})$$

Note that

$$\xi(2n\pi/\omega) = \xi(0) = z, \quad n = 1, 2, \dots \quad (\text{A-29})$$

so that

$$M(z, 2n\pi/\omega) = M(z, 0) + \alpha (n\pi/\omega) \left[1 + \frac{4w_2^2}{\omega} \left(z + \frac{w_1}{2w_2} \right)^2 \right] \quad (\text{A-30})$$

The vertical velocity of this example also leads to a maximum in the electron density irrespective of initial conditions. Furthermore, the density is quasi-periodic in the vicinity of the height $z = w_1/2w_2$, but its peak value

soon becomes smaller than the corresponding value in the case of the preceding drift velocity.

In all three examples cited it is evident that the time dependence of the night-time electron density cannot be reasonably ignored. Although the location of a peak value may remain fixed, the thickness and other characteristics of a night-time E_s layer change with a characteristic time of about an hour.

APPENDIX B

VEHICLE PERFORMANCE DATA

Nike Apaches 14.278-282 were launched from Ft. Churchill, Canada in September 1966. Nike Apache 14.77 was launched from Cassino, Brazil in November 1966 during a total eclipse of the sun. The performance of all six vehicles used in this portion of the program was good. The corresponding data for the ten vehicles used in the preceding portion of the program were given in an Interim Report (GCA Technical Report No. 66-11-N).

The predicted performance data are given in Table B-1 for the two types of payload used. The data which is based on an effective launch elevation angle of 86 deg. are included for comparison with the actual performance data listed in Tables B-2 through B-4.

The rocket launch data given in Table B-2 indicate normal flights for all vehicles and good agreement between predicted and actual time of impact. Stage ignition and burnout are also listed in this table. No data are included for Nike Apache 14.282 since this vehicle carried a TMA vapor canister but no probe nor telemetry.

The payloads on Nike Apaches 14.278-281 were instrumented with radar beacons (Vega, Model 206S). This was done as a precaution so that photography of the trails from the aircraft could proceed even though clouds prevented photography from the ground. Previous experience at the Fort Churchill Rocket Range, confirmed in the current series of flights, had shown that skin-tracking of these vehicles is unreliable.

Each vehicle was tracked by two radars (MPS-19), one for skin-track and one for beacon-track. Only partial trajectories were obtained from the skin-track method. This was the first series of flights on this program to be equipped with beacons.

The radar beacon signal of Nike Apache 14.278 was lost at $T + 190$ sec, 9 seconds after the sodium vapor release was initiated. This is attributed to condensation of sodium vapor on the quadraloop antennas of the beacon. A similar effect had previously been observed on Nike Apaches 14.194 and 14.197 where the telemetry signal was lost about 45 seconds after ignition of the sodium canister. For these two flights the telemetry signal was re-acquired late in the flight as aerodynamic heating of the surface of the insulators evaporated the metallic film which had been deposited on the quadraloop antennas. It is interesting to note that the sodium release of Nike Apache 14.278 did not result in loss of the telemetry signal. This is attributed to the change in type of antenna mounting in which the insulator is within the payload shell instead of external to it as was the case with the quadraloop antennas used in the earlier flights.

It is evident from the data of Nike Apache 14.281 that the release of TMA does not interfere with the signal from the radar beacon, just as this and previous flights had shown no interference with the telemetry signal.

The beacon track radar data provided fairly complete trajectories, except in the case of Nike Apache 14.280 where the payload beacon failed at $T + 170$ sec. However, the trajectories obtained were not sufficiently smooth to provide the accuracy required for analysis of the scientific data. Beacons were not installed in Nike Apaches 14.77 and 14.282.

The altitude and time of apogee data are given in Table B-3(a) and (b). The altitudes obtained by the time-of-flight method using baroswitches in the payload are compared with the flights for which satisfactory radar data were obtained. Good agreement is noted for apogee altitude for Nike Apaches 14.278 and 14.281 but the baroswitch value is 5.3 km lower than that obtained from radar for Nike Apache 14.279.

Precessional motion and spin rate data at apogee obtained from magnetic aspect data are given in Table B-4. Exceptionally good spin stabilization was realized for Nike Apaches 14.278-281 as may be noted by the small cone angles which range from 1.0 to 5.0 degrees. The high spin rate (7.0 to 8.4 rps) is a factor which contributes to the high degree of spin stabilization. The spin rate histories from launch up to $T + 40$ seconds are shown in Figure B-1. The predicted spin rate of 6 ± 1 rps is exceeded in all cases except Nike-Apache 14.77.

TABLE B-1

PREDICTED VEHICLE PERFORMANCE, 86-DEGREE LAUNCH ANGLE

PAYLOAD TYPE	PROBE/Na VAPOR	PROBE/TMA
PAYLOAD WEIGHT	86 lb.	74 lb.
APOGEE TIME	209 sec.	217 sec.
APOGEE ALTITUDE	525,000 ft. (160 km)	633,000 ft. (192.9 km)
IMPACT TIME	406 sec.	422 sec.
IMPACT RANGE	243,000 ft.	285,000 ft.

TABLE B-2

ROCKET LAUNCH DATA (TELEMETRY RECORDS)

 Nike Apache 14.278 (14 September 1966, Fort Churchill, Manitoba)

Nike Ignition:	0135:21.8 UT	(T)
Nike Burnout:	0135:25.3 UT	(T + 3.5 sec)
Apache Ignition:	0135:45.3 UT	(T + 23.5 sec)
Apache Burnout:	0135:52.0 UT	(T + 30.2 sec)
Impact (Loss of Signal):	0141:51.0 UT	(T + 389.2 sec)

Nike Apache 14.279 (14 September 1966, Fort Churchill, Manitoba)

Nike Ignition:	0423:00.2 UT	(T)
Nike Burnout:	0423:03.6 UT	(T + 3.4 sec)
Apache Ignition:	0423:23.1 UT	(T + 22.9 sec)
Apache Burnout:	0423:29.9 UT	(T + 29.7 sec)
Impact (Loss of Signal):	0429:57.0	(T + 416.8 sec)

Nike Apache 14.280 (16 September 1966, Fort Churchill, Manitoba)

Nike Ignition:	0122:00.1 UT	(T)
Nike Burnout:	0122:03.6 UT	(T + 3.5 sec)
Apache Ignition:	0122:23.1 UT	(T + 23.0 sec)
Apache Burnout:	0122:29.8 UT	(T + 29.7 sec)
Impact (Loss of Signal):	0129:02.3 UT	(T + 422.2 sec)

Nike Apache 14.281 (16 September 1966, Fort Churchill, Manitoba)

Nike Ignition:	0259:59.8 UT	(T)
Nike Burnout:	0300:03.3 UT	(T + 3.5 sec)
Apache Ignition:	0300:23.2 UT	(T + 23.4 sec)
Apache Burnout:	0300:29.8 UT	(T + 30.2 sec)
Impact (Loss of Signal):	0307:01.5 UT	(T + 421.7 sec)

Nike Apache 14.77 (12 November 1966, Cassino, Brazil)

Nike Ignition:	1401:59.2 UT	(T)
Nike Burnout:	1402:02.7 UT	(T + 3.5 sec)
Apache Ignition:	1402:19.4 UT	(T + 20.2 sec)
Apache Burnout:	No Data	
Impact (Loss of Signal):	1408:57.4 UT	(T + 428.2 sec)

TABLE B-3a

APOGEE ALTITUDE (RADAR DATA)*

<u>NIKE APACHE</u>	<u>APOGEE</u>	<u>TIME FROM LAUNCH</u>
14.278	156.8 km	No Data
14.279	186.2	+215 sec.
14.280	No Data	No Data
14.281	184.6	+220 sec.
14.77	No Data	No Data

*Based on plotboard data.

TABLE B-3b

APOGEE ALTITUDE AND TIME OBTAINED
FROM TIME ABOVE REFERENCE ALTITUDE

<u>NIKE APACHE⁺</u>	<u>APOGEE</u>	<u>TIME FROM LAUNCH</u>
14.278 ^{**}	156.0 km	200.5 sec
14.279 [*]	180.9	215.0
14.280 [*]	185.3	217.2
14.281 [*]	184.6	217.4
14.77 [*]	185.3	215.0

^{**}Reference altitude used is 23.0 km

^{*}Reference altitude used as 21.3 km

⁺Vehicles listed in chronological order

TABLE B-4

PRECESSIONAL MOTION AND SPIN RATE (AT APOGEE)*

Nike Apache ⁺	Precession Period (sec)	Cone Angle (degrees)	Spin Rate (rps)
14.278	29.5	4.1	7.6
14.279	37.0	2.0	7.0
14.280	33.0	1.0	7.6
14.281	30.0	5.0	8.4
14.77	40.0	9.8	6.5

* Data obtained from magnetic aspect sensor.

⁺ Vehicles listed in chronological order.

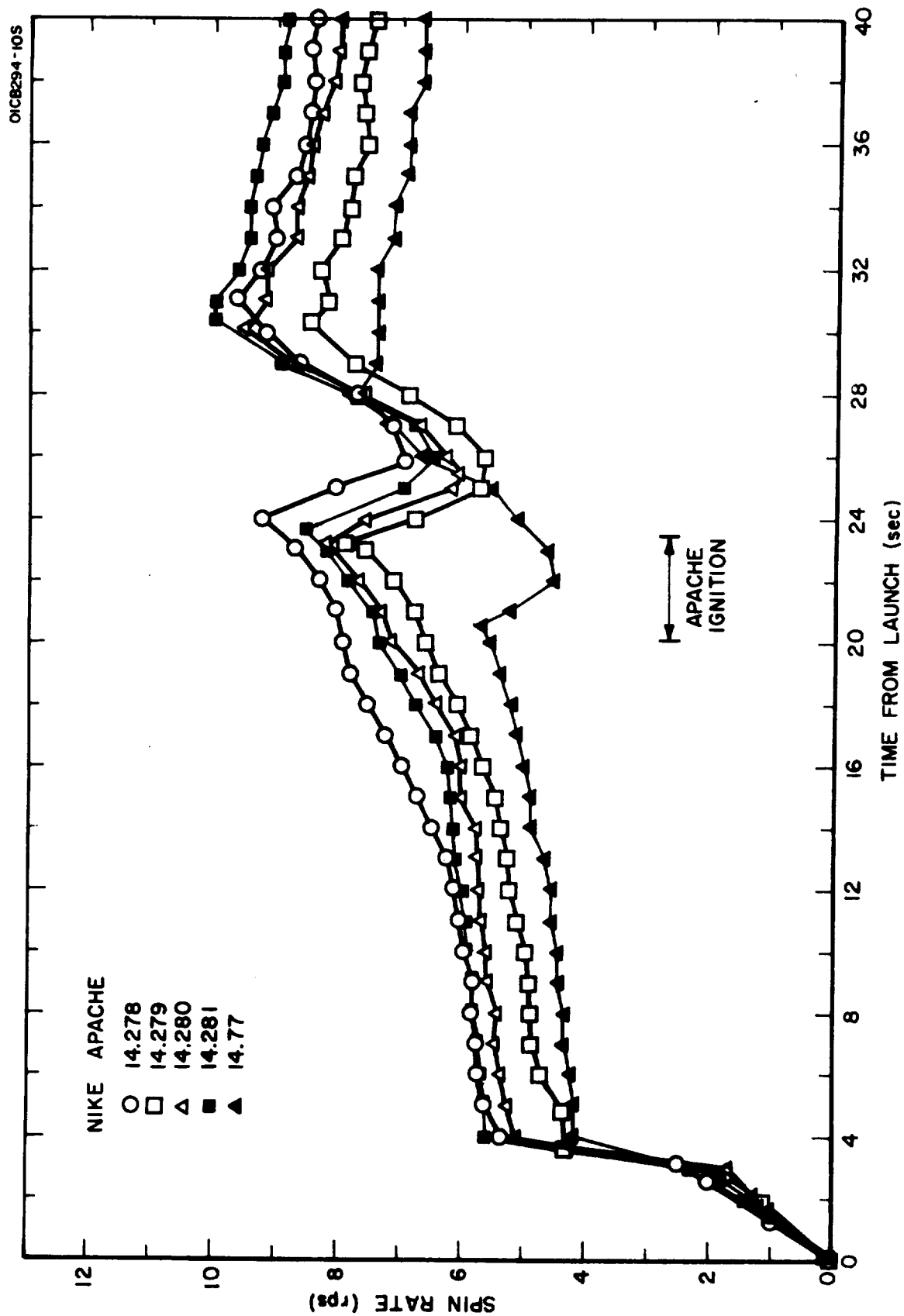


Figure B-1. Spin rate histories of Nike Apaches 14.278-14.281 and 14.77.